MICROCOPY RESOLUTION TEST CHART

NATIONAL BUREAU OF STANDARDS 1963 A

②

# the
# ohio
# state
# university

# research foundation

**1314 kinnear road**
**columbus, ohio**
**43212**

SEMICONDUCTOR SPATIAL LIGHT MODULATORS

Stuart Collins, Jr. and Marlin O. Thurston
Department of Electrical Engineering

For the Period
March 18, 1980 - June 30, 1981

**DTIC**
**ELECT**
**DEC 27 1982**

E

December, 1982

82 12 27 052

| REPORT DOCUMENTATION PAGE | READ INSTRUCTIONS BEFORE COMPLETING FORM |
|---|---|

| 1. REPORT NUMBER | 2. GOVT ACCESSION NO. | 3. RECIPIENT'S CATALOG NUMBER |
|---|---|---|
|  | AD H134237 |  |

| 4. TITLE (and Subtitle) | 5. TYPE OF REPORT & PERIOD COVERED |
|---|---|
| SEMICONDUCTOR SPATIAL LIGHT MODULATORS | Final Report 3/18/80-6/30/81 |
|  | 6. PERFORMING ORG. REPORT NUMBER 762090/712754 |

| 7. AUTHOR(s) | 8. CONTRACT OR GRANT NUMBER(s) |
|---|---|
| Gianfranco Gerosa, Jose A. Maiz, Wisik Min, Stuart A. Collins, Jr., and Marlin O. Thurston | Contract No. DASG60-80-C-0037 |

| 9. PERFORMING ORGANIZATION NAME AND ADDRESS | 10. PROGRAM ELEMENT, PROJECT, TASK AREA & WORK UNIT NUMBERS |
|---|---|
| The Ohio State University Research Foundation, 1314 Kinnear Road Columbus, Ohio 43212 |  |

| 11. CONTROLLING OFFICE NAME AND ADDRESS | 12. REPORT DATE |
|---|---|
| Department of the Army Ballistic Missile Defense Systems Command Huntsville, Alabama 35807 | June 1982 |
|  | 13. NUMBER OF PAGES 107 |

| 14. MONITORING AGENCY NAME & ADDRESS (if different from Controlling Office) | 15. SECURITY CLASS (of this report) |
|---|---|
|  | Unclassified |
|  | 15a. DECLASSIFICATION DOWNGRADING SCHEDULE |

16. DISTRIBUTION STATEMENT (of this Report)

Approved for public release; distribution unlimited.

17. DISTRIBUTION STATEMENT (of the abstract entered in Block 20, if different from Report)

18. SUPPLEMENTARY NOTES

19. KEY WORDS (Continue on reverse side if necessary and identify by block number)

Light-valves, Optical, Modulation, Switching

20. ABSTRACT (Continue on reverse side if necessary and identify by block number)

The objective of this research was to evaluate techniques for modulating or switching one beam of light with another. The processes investigated were free carrier Faraday rotation, sensor-controlled optical emission, modulation of magnetic bubble diameter, selective pumping of an excited state in garnet with circularly polarized light, and modulation of optical absorption in silicon by pumping hole states. In the last method a control beam of wavelength 1.06 micrometers was used to modulate the transmission and reflection of a 10.59 micrometer beam.

DD FORM 1473 1 JAN 73 EDITION OF 1 NOV 65 IS OBSOLETE

Semiconductor Spatial Light Modulators

Stuart Collins, Jr.
and
Marlin O. Thurston

The Ohio State University
Department of Electrical Engineering

TABLE OF CONTENTS

LIST OF TABLES

iii

LIST OF FIGURES

LIST OF FIGURES, Contd.

# 1. INTRODUCTION AND OBJECTIVES

Sources of coherent infrared radiation, such as the 10.6 micrometer laser, have become increasingly important in systems. Consequently there is a need to find improved techniques for beam control and image or signal processing. For example, there is a liquid crystal cell, but not at present an optical spatial light modulator (SLM) capable of operating in real time in the 3-12 micrometer wavelength range.

Optical spatial light modulations were developed to transfer incoherent optical images onto a coherent light beam. Their use has led to the meaningful application of real-time Fourier-based optical signal processing systems. If such a spatial light modulator were available for the infrared there would be significant application there also. One might be artificially beam steering or focussing using the SLM as an optically controlled diffraction grating or Fresnel lens. This has been demonstrated by Christensen [1] and could have obvious applications in an imaging array receiver used for star system identification. Another application might be object identification by pattern recognition in a 10.6 micron imaging system. Such identification has been aptly demonstrated in the visible spectral range by Gara [2] using indoor scenes and by Christensen [3] using outdoor scenes. Both workers used a slow Hughes Liquid Crystal Light Valve type of SLM.

In yet another area, effort has been put into the development of numerical optical computing using residue arithmetic [4]. The best approach involves the application of a fast optical spatial system using a cyclic optical variable, the residue arithmetic being basically cyclic. A numerical optical spatial computing system using a birefringence-based

1

liquid crystal light valve has been developed but is slow. A
semiconductor-based spatial light modulator using optical Faraday
rotation would also have the advantages of optical spatial systems,
namely high information density and parallel processing, in addition to
the cyclic variable for residue arithmetic and the speed that other
systems lack.

The objective of this research was to review proposed methods for
achieving optical spatial light modulation and to make experimental
studies of the most promising approaches.

## 2. REVIEW OF SELECTED OPTICAL MODULATION PROCESSES

### 2.1 Franz-Keldysh modulators

One class of electro-absorption infrared modulators is based on
the Franz-Keldysh effect. This effect is a variation of bandgap of a
semiconductor produced by means of a high electric field. Devices in
practical use are capable of an attenuation range of about 60 dB and have
switching times in the microsecond range. These devices are essentially
small optical waveguides of the order of a millimeter in length. The
transmission path is a compound semiconductor with a bandgap energy
slightly greater than the photon energy of the radiation to be transmitt-
ed. When a sufficiently large electric field is applied perpendicular to
the guide, the bandgap is reduced enough to allow photon absorption [7].
The physical embodiment would be an array of small optical waveguides
absorbing light at one angle and radiating spatial modulated light in
another direction. The advantages of this system are the existence of
the technology and the wide dynamic range. Disadvantages are the
circuit-imposed limitations on speed and the geometrical problems in

design of arrays. The necessity for electrical, rather than optical, control of the modulation may be a disadvantage, particularly in view of the problem of addressing individual cells. For these reasons we did not investigate these devices further.

## 2.2 Sensor-controlled emission techniques

As the name suggests, such techniques refer to the emission of radiation from a source that is controlled by light falling on a sensor. In the simplest implementation a light-emitting diode on one side of an opaque plate might be connected to a phototransistor on the other side of the plate. Such an arrangement would, of course, require a dc power supply. The intensity of the emitted light could be made higher than that of the controlling light. The emitted light could also be of quite different wavelength from controlling light. If laser diodes were used there could be a conversion from incoherent to coherent light.

In order for this sensor-amplifier-emitter combination to be useful in a spacial light modulator it would have to be produced in an integrated array. Such an array has been made by Beneking et al. [8] using layers of compound semiconductors deposited by molecular beam epitaxy.

Since we lack the equipment capability for growing complex hetero-structures, we made a preliminary study of the feasibility of conventional integration methods. As a guide we made several optical logic gates as well as amplifiers using discrete components. The approach is interesting for several reasons. The electronics of a cell can be complex while maintaining optical inputs and outputs. Since the output and input are coupled, the addressing problem of the Franz-Kedysh array is avoided. The dimensions of a cell might be as small as a few microns and thus the resolution might be adequate for many purposes.

3

There are, however, practical difficulties in making integrated arrays of this type. They stem mainly from the need for optical isolation between elements. These difficulties made it clear that making such an array was beyond the scope of this program. Nevertheless the fundamental advantages of electronic versatility in an optical system might justify further work.

2.3 Free Carrier Faraday rotation in semiconductors

Free carrier effects in semiconductors can also be used for optical modulation. The basic idea is that high purity GaAs, for example, is quite transparent for infrared radiation in a band with wavelength greater than about 1.0 micron. If free carriers are introduced by injection or radiation, two effects may be observed. Radiation at a longer wavelength, e.g., $10\mu$, will be absorbed in proportion to the free carrier concentration. In addition, if a magnetic field is applied in the direction of beam transmission, there will be a Faraday rotation of the angle of polarization.

If an intense beam of light of wavelength $0.9-1.0\mu$ is used to generate free carriers, it may be considered to be the control signal. This control signal can then be used to amplitude modulate a $10\mu$ beam either with or without a magnetic field. If a magnetic field is present, it should be possible to use two coincident control beams to achieve logic functions.

A simplified theoretical model was presented in the original proposal submitted on March 28, 1979. Expressions for the rotation per unit length and absorption per unit length were obtained from Moss [9]. Since then a complete derivation has been obtained where classical physics has been used as a starting point, with the results which are stated here:

4

$$\alpha = \frac{q^3 \lambda^2}{4\pi^2 n C^3 \epsilon_0} \left[ \frac{n(x)}{\mu_n m_e^2} + \frac{p(x)}{\mu_p m_n^2} \right] \qquad (1)$$

$$\kappa = \frac{\lambda}{4\pi} \alpha \qquad (2)$$

$$\theta_{fc} = \frac{-q^3 B_z \lambda^2}{8\pi^2 \epsilon_0 C^3} \frac{n}{n^2 - \kappa^2} \left[ 1 + i \frac{\lambda \alpha}{4\pi n} \right] \cdot \left[ \frac{n(x)}{m_e^2} - \frac{p(x)}{m_n^2} \right] \qquad (3)$$

where  $\alpha$ = absorption coefficient per unit length

$q$ = electron charge

$\lambda$ = wave length of infrared radiation

$n$ = index of refraction of semiconductor

$C$ = speed of light

$\epsilon_0$ = permittivity in free air

$\mu_n$ = electron mobility

$\mu_p$ = hole mobility

$m_e$ = electron effective mass

$m_n$ = hole effective mass

$\theta_{fc}$ = free carrier Faraday rotation in RAD/cm

$B_z$ = applied magnetic field

$n(x)$ = electron concentration in 1/cc

$p(x)$ = hole concentration in 1/cc

In addition the figure of merit can be expressed as $\theta_k/\alpha$.

A few comments can be made about equations (1) through (3).
First, it should be mentioned that the optically excited electron and
hole populations give rise to the Faraday effect are not uniform.  Their

5

concentration profiles are usually exponential with an associated characteristic diffusion length. Furthermore, most semiconductors have some type of initial doping. As a result, $n(x)$ is the addition of the background level of free electrons and the optically excited ones. Secondly, the Faraday effect contains real and imaginary parts. The real part is the expression for a real rotation while the imaginary part is an expression for a real rotation while the imaginary part is an expression for the ellipticity of the rotated infrared beam. This ellipticity is directly proportional to the absorption coefficient which is rather low even for moderate levels of photo excitation.

Several conditions are to be met to satisfy the above expressions. These include:

1) $\lambda > \lambda_g$ where $\lambda_g$ is the absorption edge wavelength of the semiconductor

2) $\lambda^2 \ll (\pi m^* c)^2 / (q B_Z)^2$ for $B_Z$ up to 10 kGass this condition can be easily met.

## Optical Generation of Free Carriers

The bulk rate of carrier generation at a plane situated at a distance x from the illuminated surface of the semiconductor is given by [10]

$$g(x,t) = \alpha \gamma_\lambda (1-R_\lambda) I_0(t) e^{-\alpha x} \qquad \text{carriers/sec-cm}^3 \qquad (4)$$

where $\alpha$ : absorption coefficient in 1/cm

$\gamma_\lambda$ : quantum efficiency

$R_\lambda$ : reflection coefficient of incident radiation

$I_0(t)$ : number of photons/sec·cm$^2$ at incident surface

The 2nd order time-dependent differential equation that describes the motion of free electrons and holes in a semiconductor is given by [11]

6

$$\frac{\delta n}{\delta t} = D \frac{\delta^2 n}{\delta x^2} - \frac{n-n_0}{\tau} + g(x,t) \tag{5}$$

where  n : electron-hole pairs generated

   D : diffusivity of carriers

   $n_0$ : thermal equilibrium carriers

   $\tau$ : carrier lifetime.

The solution to the above equation where the radiation pulse-width is much larger than the carrier lifetimes and surface recombination is accounted for in a semiconductor slab or wafer is,

$$n(x)-n_0 = \frac{\alpha I_0 \tau}{(L\alpha)^2 - 1} \cdot \left[ A\epsilon^{-x/L} - \epsilon^{-\alpha x} + B \right] \tag{6}$$

where

$$A = \frac{s + \frac{\alpha L^2}{\tau}}{s + \frac{L}{\tau}} \cdot \frac{1 + \epsilon^{-\alpha d}}{1 + \epsilon^{d/L}} \tag{7}$$

and

$$L = \sqrt{D\tau} = \sqrt{kT\mu\tau/q} \tag{9}$$

and    s = surface recombination velocity in cm/sec

   d = sample thickness.

Although the above solution is general, it does not account for multiple internal reflections that exist within the slab for incident photon energies which are just under the semiconductor's band gap energy.

One can deduce from the above formulations that due to the gradients that exist in the photo-excitation of carriers along with surface recombination phenomena, the Faraday effect will be much lower

7

than anticipated. Figures 1 and 2 show the carrier distribution in a 250 micron indium antimonide wafer for several input laser power densities ($n_\lambda = 1.0$) and two different surface recombination velocities. Figure 3 shows the carrier distribution for a Gallium-Arsenide sample. The photo-excited carriers decay in GaAs in a shorter distance because of their lower diffusion lengths as compared to InSb.

Using equations (1) - (9) the real part of the Faraday effect was obtained for InSb as a function of incident radiation power densities. Figure 4 shows the angle of rotation for two temperatures in InSb. Figure 5 shows the Faraday effect in GaAs.

Reduction in mobilities and lifetimes due to the high levels of carrier concentration at high input powers have not been taken into consideration. As a result, the expected results for the Faraday effect should be lower than portrayed by Figures 4 and 5.

The Faraday effect is greater in InSb than in GaAs as Figures 4 and 5 show. This is a direct result from the fact that the electron effective mass is smaller in InSb. In addition, the carrier diffusion lengths are longer in InSb; thus moderate levels of photo excited carriers can be sustained for longer distances.

As we have seen, large powers are required from the control radiation to obtain practical angles of rotation. To increase the Faraday effect the applied dc magnetic field may be increased at the expense of more power applied to the overall system. The proposed alternative is a type of multi-pass device where the infrared radiation to be rotated is forced to transverse the semiconductor before it exists. In effect, the $\lambda$ parameter in
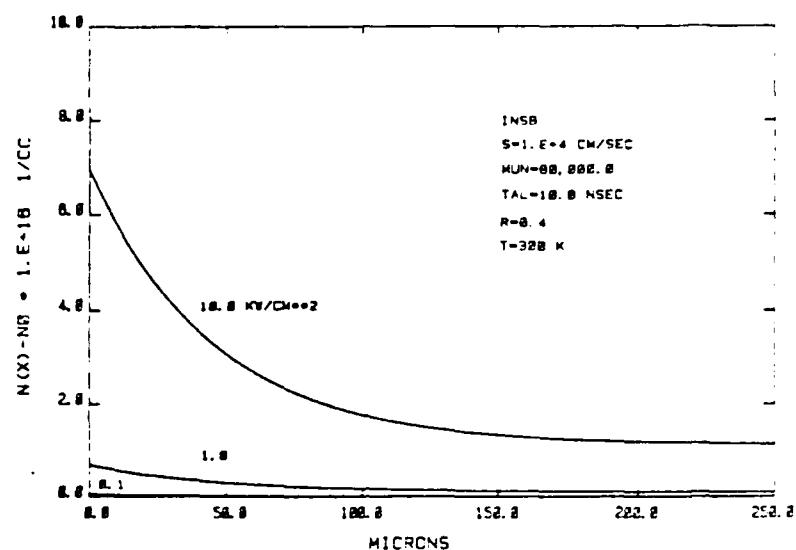
FIGURE 1.   Carrier Distribution with Low Surface Recombination
            and Wavelength 0.904 um.
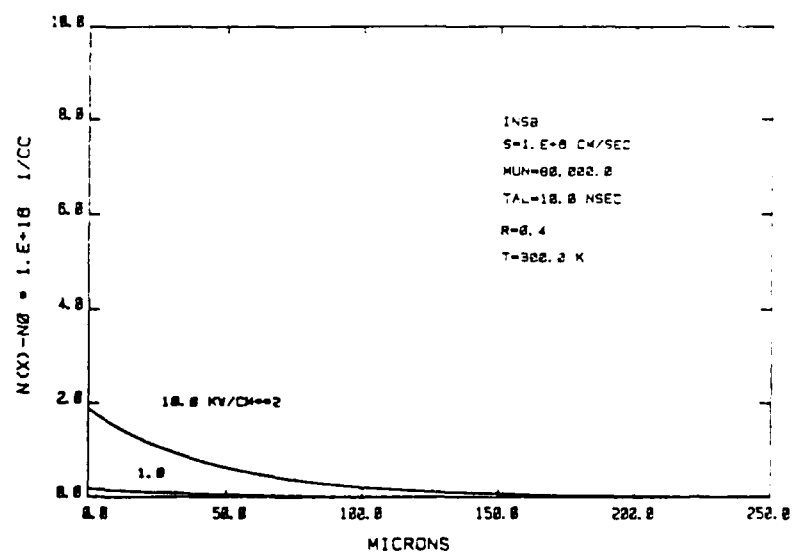


FIGURE 2. Carrier Distribution with High Surface Recombination and
          wavelength 0.904 µm.

9
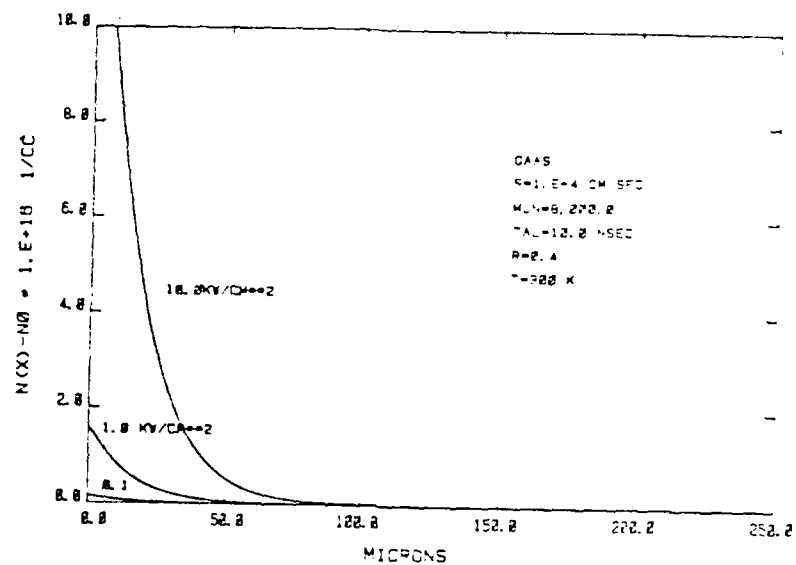
FIGURE 3. Carrier Distribution with Low Surface Recombination and Wavelength 0.850 um.

10
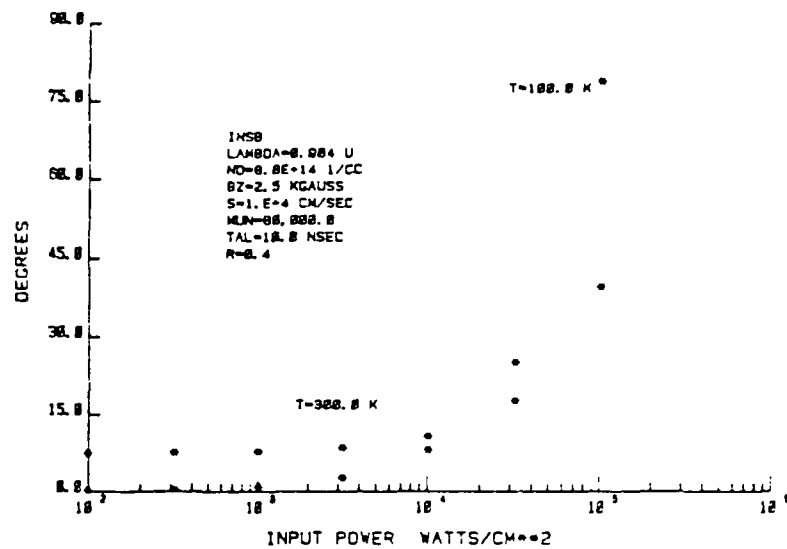
FIGURE 4. Faraday Rotation, InSb.
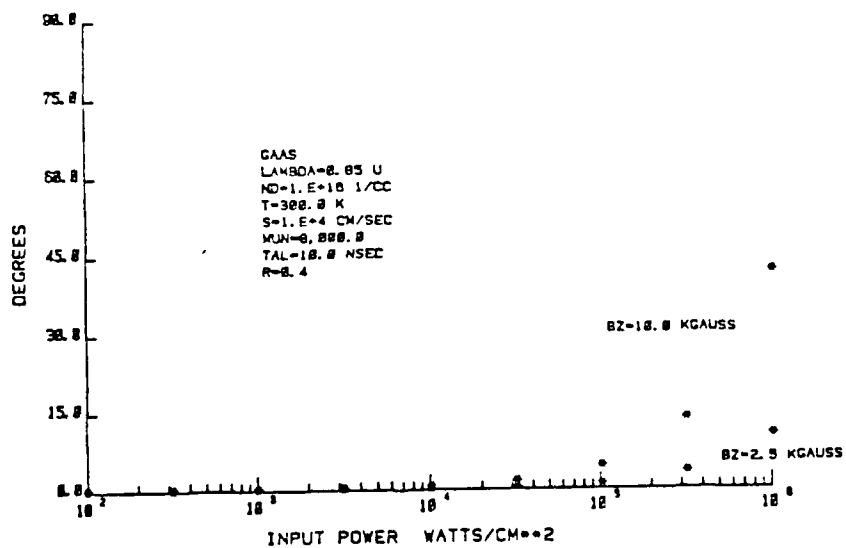


FIGURE 5.   Faraday Rotation, GaAs.

11

$$\Theta = V \cdot B \cdot \ell$$

is being increased where V, the verdet coefficient, and B, the applied dc magnetic field, are unchanged. The multi-pass device functions as a semiconductor waveguide.

To provide a practical picture of the increased effect in a multi-pass device where a spot size of 3mm x 3mm in InSb at T = 100°K is used as a basis for comparison.

$\lambda$ = /905 microns       (control beam focused in an area ~0.1 cm$^2$)

P = 100 W

s = 10$^4$ cm/sec

t = .5 mm

$N_0$ = 9x10$^{14}$ atoms/cc

n(x) = uniform level

The comparative Faraday rotations for the conditions specified above are as follows:

|  | SINGLE PASS | MULTI-PASS ($\alpha$ internal 16°) |
|---|---|---|
| $\Theta_{off}$ | 0.13° | 2.5° |
| $\Theta_{on}$ | 1.4° | 28.0° |

The advantage of a multi-pass configuration rests on the total increase in length that the signal beam is to travel. This length can be expressed as,

$$\ell = \frac{d}{\sin \alpha}$$

where d is the control beams spot size, and $\alpha$ is the angle of internal reflection. $\alpha$ must be greater than the critical angle which is equal to 14.5° for InSb.

12

Because of the several passes that the infrared beam takes,
regions of high carrier levels, which are usually close to the surface,
will be tranversed many times.  As a result, not only is $\ell$ being
increased, but V which is directly proportional to carrier level will
also be increased.

Several problems need still to be studied for the multi-pass
device:  coupling devices and their efficiencies, radiation angle
sensitivities, increased attenuation of the signal beam, and element size
optimization for integration purposes.

## 2.4  Optical Modulation with Magnetic Garnets

Magnetic garnets are materials that can produce large rotations of
the polarization plane of the light while maintaining an acceptable
transparency.  They appear very attractive for applications in devices
like spatial light modulators and optical gates provided that the Faraday
effect can be modulated by external means, preferable optically.  Differ-
ent attempts to achieve that are found in the literature, like using
waveguides of garnet and an external magnetic field to cause the switch-
ing [12] or using a laser beam to move and manipulate magnetic bubbles or
domains [13].

To be useful as spatial light modulators or gates for optical
computing the modulation scheme must be easily integrated into an array
and controlled in parallel.

13

Two of the approaches we studied were:

a)  to provide localized magnetic fields to
control the direction of magnetization
of the garnet and thus change the sign
of the rotation

b)  to modulate some basic parameter  of
the material which affects the amplitude
of the rotation.

a)  The basic idea in this study was to produce a rectangular array of magnetic bubbles in a plate of garnet and to remove or create individual bubbles by optical means.  The mechanism proposed was to surround each bubble location with a conducting ring in which a current could be used to produce the necessary local magnetic field.  Two methods were considered:  One was to place a photovoltaic diode in each ring and the other was to place a photoconductor in each ring.  In either case a beam of light on the cell could be used to switch the bubble. (Fig. 6)

The material most extensively used in our study of the effects of local magnetic fields has been $Gd_{2.1}Bi_{0.9}Fe_{4.6}(GaAl)_{0.4}O_{12}$ with a thickness of 4.7 $\mu$m [14].  The Faraday rotation for this sample can be seen in Fig. 7 and its transmission in Fig. 8.

Since the compensation temperature is 281°k the saturation magnetization constant at room temperature is small and external magnetic fields of $17 \times 10^{-4}$ Tesla are enough to reverse the Faraday rotation in the whole sample.  A strong hysteresis has been observed in this material and once it is oriented in one direction, it will stay oriented in that direction until a magnetic field in the opposite direction is applied.

14
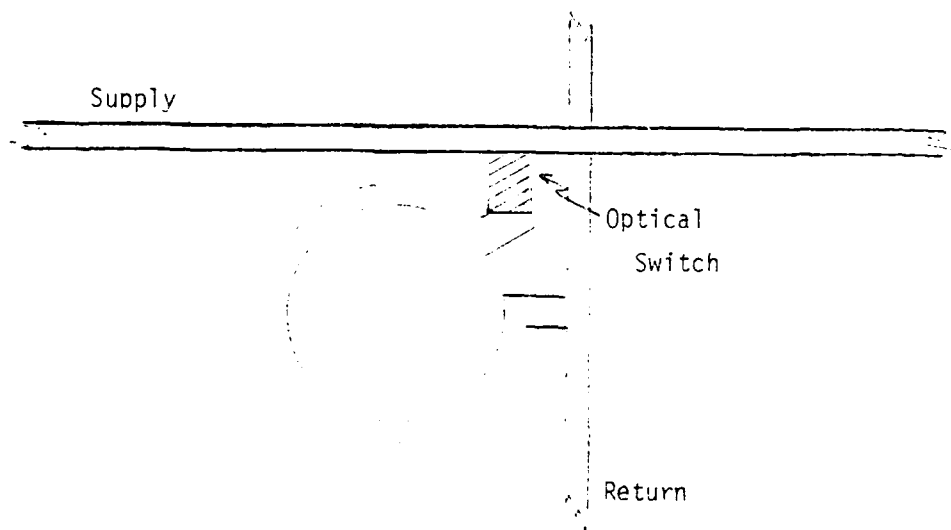
Figure 6    Magnetic bubble cell.
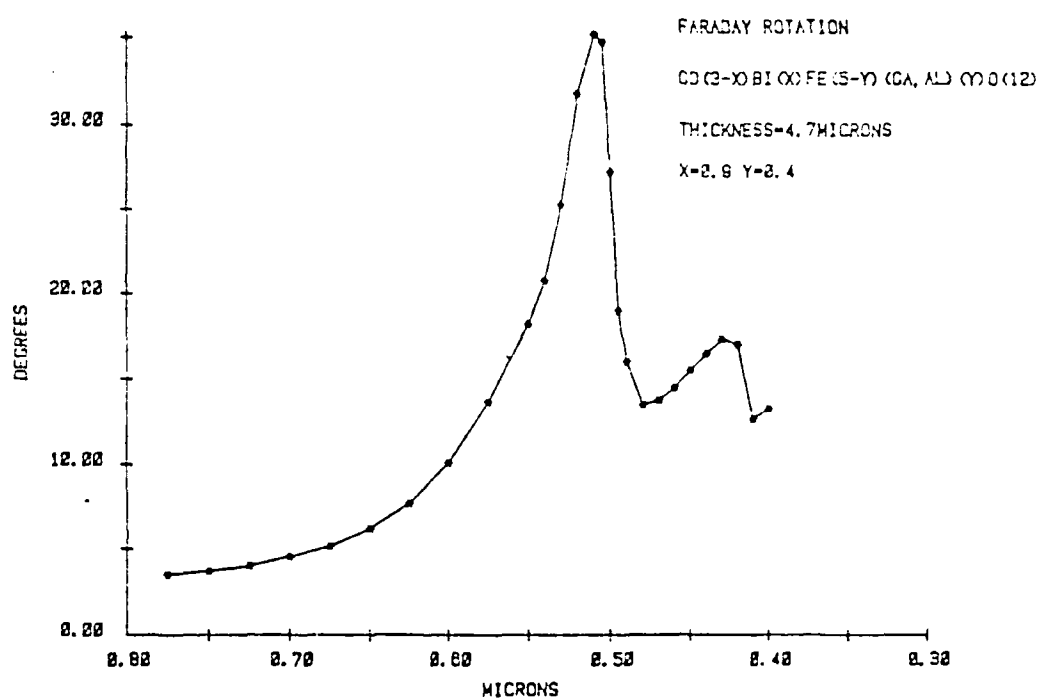
FIGURE 7    Experimental Faraday Rotation in Sample Garnet.
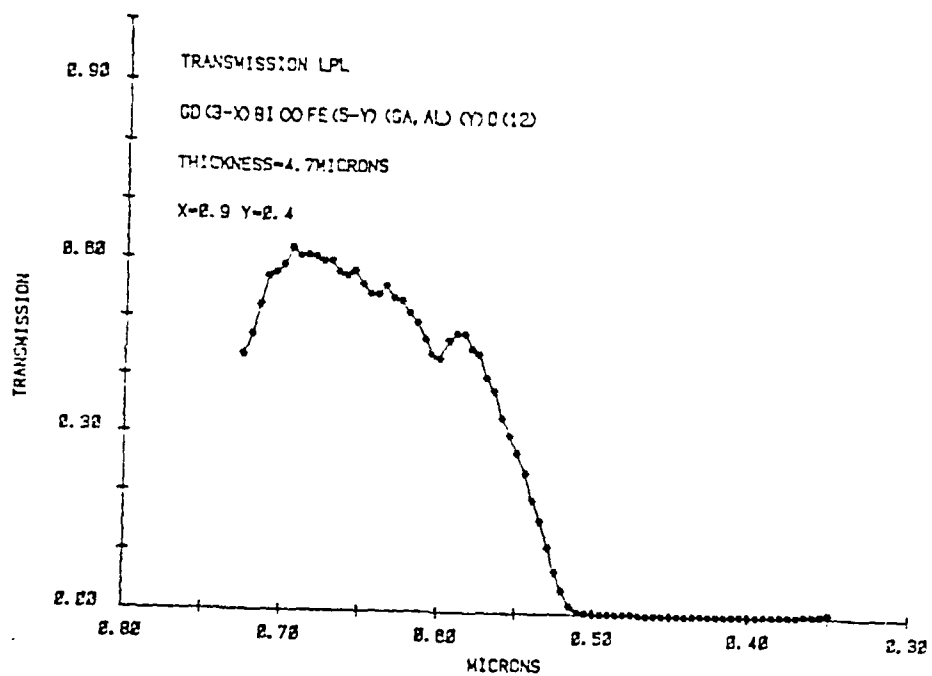
FIGURE 8   Experimental Transmission Coefficient in Sample Garnet.

17

Photolithographically defined metal microcircuits have been used to generate magnetic fields locally. The first idea was to produce a local magnetic field large enough to locally reverse the direction of the magnetization in the garnet but the currents needed are too large. What appears to be a much better approach is to provide for a nucleation point in or near the active element defined in the garnet. This way magnetic fields between 10-15 oersted should be enough to cause the switching for a given active element. It has been observed that evaporating a very small area of aluminum near the garnet produces a very effective nucleation point. The nucleation points are defects that help to start the reversal of the magnetization. Since reduction in the thickness of the garnet reduces the energy per unit area of domains whose magnetization is opposite to the external magnetic field the etching of small areas defined photolithographically should provide for nucleation points. Another way to produce a nucleation point in garnets with composition $Eu_{2.8}Bi_{0.2}Ga_{0.6}Fe_{4.4}O_{12}$ is to evaporate small dots of gold and anneal the sample at 500°C for 15 minutes in a forming gas atmosphere. However, this procedure has produced cracks in the surface of the garnet, damaging the sample.

It thus appears possible to make a two dimensional array of optical gates by using a pattern of nucleation points on garnet in register with a pattern of semiconductor current loops. An attempt was made to fabricate the current loops using a silicon-on-sapphire process. Since a current pulse of the order of 30 mA is needed to switch a garnet region 30 µm in diameter, the design is not simple. Although we were not able to demonstrate a working device with our facilities in the time available, the idea may warrent further study.

18

Our investigation of the second approach was based on the well-known rotation of the plane of polarization of a linearly polarized beam of light that occurs when it transverses a slab of material and its photon energy is close to a transition in which at least one of its levels, either the ground or the excited state, is a multiplet and it has been split (Zeeman effect) by a magnetic field either internally generated or externally applied. In addition to the usual parity, spin and total angular moment conservation, the conservation of the total magnetic moment determines whether a specific transition between sublevels is going to be allowed or forbidden for each of the components of the incident beam, that is, linear right circular and left circularly polarized. The simplest case arises when the ground state is a singlet (S state) and the excited state is a triplet (P state) (Fig. 9).

If we consider the incident linearly polarized beam as composed of right and left circularly polarized components, the allowed transitions for both of them correspond to different energy values and thus their index of refraction and their absorption coefficients will be different, resulting in a rotation of the plane of polarization for the outgoing beam and also some degree of ellipticity. The specific rotation depends among other factors on:

```
                          ————————  m = 1
P   ——————————————————————  m = 0
                          ————————  m = -1


S   ——————————————————
```
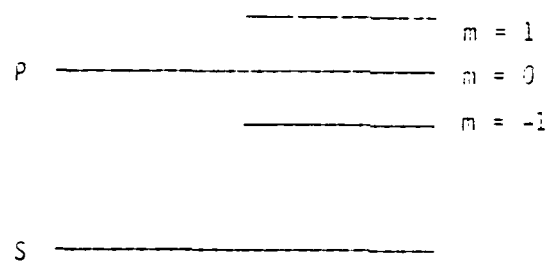
FIGURE 9.  Typical Energy States.

1) Separation of the two active sublevels

2) Energy separation between the beam and the center
   of the transition

3) Linewidth

4) Transition probabilities

5) Population of ground and excited levels

Modulation in various degrees can be achieved by externally affecting any of the mentioned factors and each one could be considered a different approach. The two approaches considered in this work are:

a) Coherent excitation which is directed to factor 2

b) Incoherent excitation which is directed to factor 5.

a) -- Coherent excitation can be achieved when the material has a very narrow absorption line and it is pumped by a circularly polarized dye laser beam whose monocromaticity is good enough so that it can be tuned very close in energy to the absorption line but without being significantly absorbed. Under these conditions the electrons are excited coherently and their energy levels are shifted in a process that has been called adiabatic following [15]. This produces large changes in the Faraday rotation effect of a linearly polarized beam whose energy is in the vicinity of the absorption peak. The responses are very fast (picoseconds) and by adjusting the frequencies, the controlled beam can be made much higher in power than the controlling beam, thus providing gain.

b) -- Incoherent excitation. The previous scheme might not be possible in the case where the absorption line is not very narrow. Thus the idea here is to pump the system with a circularly polarized beam tuned at the center of the line. The absorption of the beam pumps electrons from the ground level to one of the excited levels changing the electron populations and producing large changes in the Faraday rotation of another beam tuned to a frequency close to the absorption line. It has been shown [16] that changes of around 10% in the population of the ground state are expected to produce changes of over 200% in the Faraday rotation effect of some garnet materials.

The material chosen for the initial tests was a magnetic garnet with composition $Gd_{2.1}Bi_{0.9}Fe_{4.6}(GaAl)_{0.4}O_{12}$, 4.7 µm thick, epitaxially grown in a non-magnetic substrate. The reason for the choice was that is very large Faraday effect suggested a large separation between sublevels, provided high Faraday effect in regions of considerable transparency, and no external magnetic field was necessary.

A study of its optical properties (absorption, reflection, Faraday effect, etc.) showed that its rotation mechanism was of the diamagnetic type (as in Fig. 9) and the separation between the absorption peaks of both active sublevels was large. Nevertheless the absorption peaks were very wide due to inhomogeneous broadening and it was clear that coherent excitation would not be significant.

Incoherent excitation was attempted in order to partially change the relative populations of the ground and excited levels. This attempt failed because the lifetime of the excited electrons was extremely short (<1 nsc) possibly due to spin-spin relaxation between the sublevels of the excited state. This made it impossible to populate one of the excited state sublevels enough to observe the desired effect despite the

22

Anti-reflection
coating for the
control beam

Semiconductor

Control beam
$\lambda = 1.06$ μm

Signal beam
$\lambda = 10.59$ μm
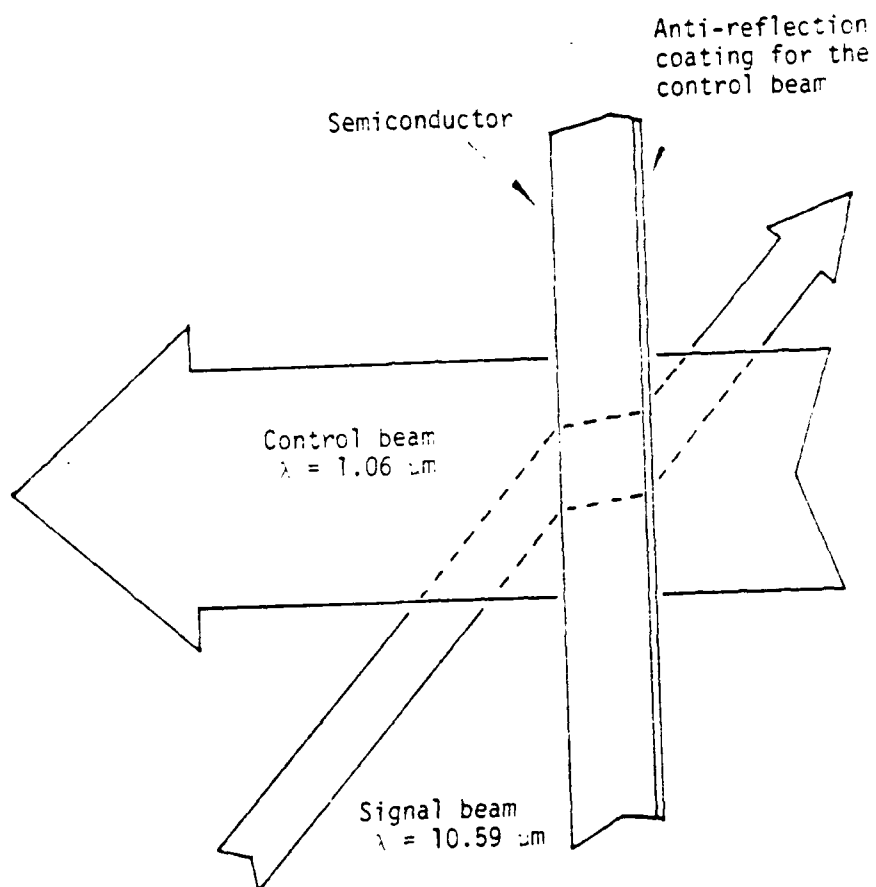
Figure 10  Optical light modulator based on
a semiconductor crystal.

fact that the laser power density was increased to levels that damaged the surface of the garnet. An attempt to find materials with more suitable energy level configuration has not yet been successful.

2.5 Modulation of optical absorption and refelction by pumping of hole states.

Infrared light modulation using semiconductors is not new. Practical devices have been made where the excess carriers are generated by minority carrier injection by a p-n junction. Germanium (Ge) was used in early modulators [17]. To improve on its switching time researchers have studied other modulators based on direct band-gap materials such as Indium--Antimonide [18] (InSb) and Gallium-Arsenide [19] (GaAs). Nonetheless, these modulators required the fabrication of p-n junctions to generate the holes needed for light absorption near ten microns ($\mu$m). Other researchers have been able to modulate light utilizing another light source and a host semiconductor. Specifically, 10.6 $\mu$m radiation modulated by a pulsed ultraviolet laser with a wavelength of 0.3371 $\mu$m has been demonstrated in GaAs [20]. An SLM based on this approach would almost be impossible due to its complex arrangement. Germanium couplers are utilized to direct a 10.6 $\mu$m beam in and out of a 2.0 millimeter long GaAs waveguide. More recently, modulation of 3 $\mu$m light by 10 $\mu$m light in p-type Germanium was shown [21]. Specifically, the transmission of the 3 $\mu$m laser beam is increased by the saturation of states on top of the valence band by the 10 $\mu$m light. A practical modulator may not result using this scheme due to the rather large control beam energy densities ($\approx$ 0.5

24

joules per squared centimeter). A simpler approach to obtain an infrared SLM would be to optically excite free electrons and holes using a control laser emitting photons with energies slightly larger than the semiconductor's band-gap energy. In turn, these free carriers absorb the 10 μm radiation. It has been shown that the dominant absorption mechanism for light having a wavelength near 10 μm is direct sub-band transitions within the valence band [22,23]. As a result, low levels of optically excited holes are sufficient to provide reasonable modulation depths. Consequently, required control energy densities are expected to be low.

A simple representation of an optical light modulator based on the absorption of light by optically excited free carriers is depicted in Figure 10. Specifically, 1.06 μm light supplied by a pulsed laser is to be used to control the intensity of 10.59 μm light within a host semiconductor. Silicon is chosen for this application because of its low absorption coefficient at the 1.06 μm wavelength. As a result, a uniform distribution of carriers can be generated by the controlling laser. This in turn, maximizes the absorption of the 10.59 μm radiation which is directly porportional to the product of the number of free holes and its optical path length. Other materials with faster recombination lifetimes (i.e. direct band-gap semiconductors) or silicon with gold centers can be used to increase the modulator's switching speed.

In Section 2.51, the theoretical analysis describing the interaction of both electromagnetic radiations with the host semiconductor is presented. This theory is separated into three parts; carrier generation by 1.06 μm light, carrier redistribution and decay, and finally, 10.59 μm light absorption. The resulting equations are derived from the fundamental relations such as Maxwell's equations for the carrier generation

25

and absorption theory, and the continuity equations for the carrier recombination theory. Infrared absorption is described by the exponential decay of photon flux with distance into the semiconductor. Finally, a brief discussion of carrier redistribution parallel to the sample's surface plane is presented. This treatment provides insight into resolution limitations in a proposed SLM based on this infrared light-controlled optical-modulator.

In Section 3.2 the experimental apparatus utilized and the method of data collection is described. The experimental configuration is presented in which a silicon wafer is simultaneously irradiated by the controlling beam and the probing beam. The sample is adjusted for Brewster's angle of incidence of the 10.59 μm beam whereas the 1.06 μm controlling beam enters the sample from the opposite surface normal to it. Also presented is a comparison between theoretical and experimental results. In addition, an improved optical modulator with a faster response time is included. Finally, the results of preliminary resolution studies of a silicon-based SLM are shown.

Finally, Section 4 contains a review of important aspects of the work. In addition, recommendations are made for further studies including proper resolution studies for a spatial modulator. Furthermore, proposals for additional work are made where other semiconducting materials could replace silicon as the host crystal in an optical spatial light modulator.

The mathematical details of the discussions are presented in a series of appendices. The redistribution of the photo-excited carriers is described by an ambipolar diffusion equation. The derivation of the

time-space solution of such equation is covered in Appendix A. The
mobility and diffusivity of these carriers are dependent on several
parameters including carrier density level. Appendix B covers the
complete formulation of an equation describing mobility as function of
carrier density. Finally, Appendix C groups all of the computer programs
utilized in this work. Data acquisition programs are also included.


### 2.5.1 Theoretical investigation

Semiconductors may be used as host crystals where electromagnetic
radiation can interact with other radiation to obtain optical switching.
By stimulating the crystal with an incident light pulse, electron-hole
pairs are generated provided that the photon energy is larger than the
semiconductor's band-gap energy. A second electromagnetic wave traveling
within the semiconductor sample whose photon energy is much less than the
band-gap energy would then be absorbed. Several absorption mechanisms
are present when the probing beam's wavelength is near ten microns.
These include phonon absorption, free carrier absorption, indirect free
hole transition, and direct intravalence transition. As the excited free
carriers return to their equilibrium state by recombining, the probing
electromagetic radiation returns to its steady-state value. As a result,
optical switching is obtained.

The purpose of this section is to develop theory that relates the
intensity of a control beam pulse to the transmission and reflection of a
probing beam via the electron-hole pair recombination within a silicon
crystal. In part A, the generation of electron-hole pairs as a function
of the control beam's intensity and transmission is developed.

27

Since the photon energy of a Nd:YAG laser is slightly greater than the band-gap of silicon, it is assumed that for every photon absorbed, one electron-hole pair is generated. Furthermore, since the absorption coefficient in silicon at 1.06 $\mu$m is less than 100 cm$^{-1}$, the control beam's energy will not be absorbed within a few microns of the crystal's surface.

In part B, a solution to the diffusion equation is developed for which the electron-hole distribution found in section A is the initial condition. A simple diffusion equation is obtained provided that the excited electron and hole concentrations and their respective first and second derivatives are approximately equal.

In part C, an explanation is given describing the absorption of 10 $\mu$m light in semiconductors. A graphical representation of the allowed optical transitions in p-type silicon is included. These absorption mechanisms are grouped together in an exponential form to obtain the transmission expression for the infrared probing beam.

Finally in part D, a two-dimensional expression describing the diffusion of optically pumped electron-hole pairs along the plane perpendicular to the direction of light propagation is presented. Since two-dimensional image processing can result from such optically controlled infrared modulators, phenomena that might limit spatial resolution is investigated. Specifically, generated carriers will diffuse away from the spot of incidence with a characteristic lifetime and diffusivity resulting in image 'smearing'. A set of two-dimensional graphs are included for various carrier lifetimes.
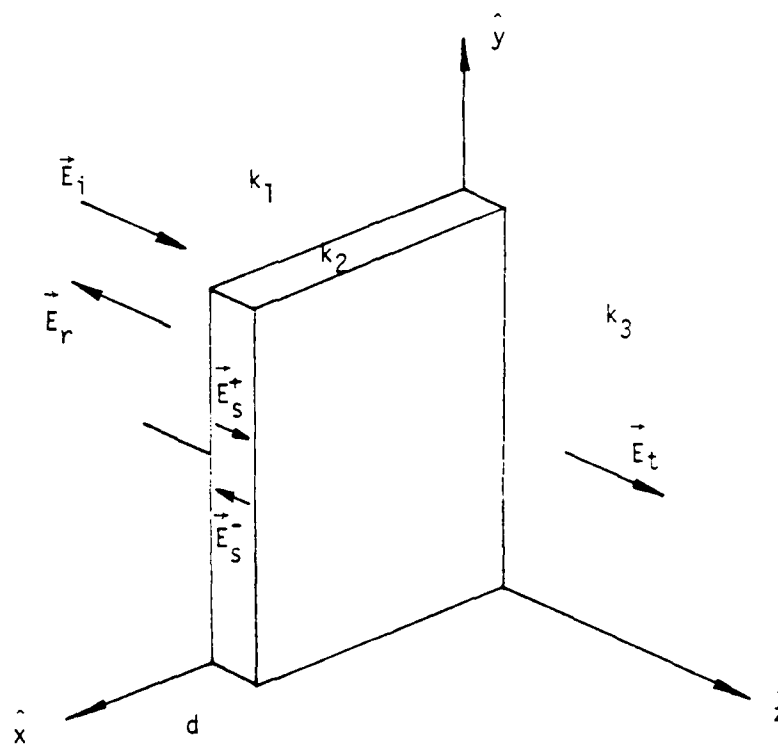
Figure 11    Reflection and transmission of 1.06 μm
light by a semiconductor slab at
normal incidence.

## A. CARRIER GENERATION

Electron-hole pairs are generated within the silicon crystal when it is exposed to a light pulse of wavelength equal to 1.06 μm. This short burst of energy is thus absorbed as it propagates through the crystal. The number of free carriers per unit volume can be obtained as a function of the control beam's incident, reflected, and transmitted intensities.

Three homogenous media can be characterized by their propagation factors $k_1$, $k_2$, and $k_3$ as shown in Figure 11. Regions 1 and 3 represent free space while region 3 depicts the semiconductor sample of thickness d. The electromagnetic fields in media one through three are,

Region 1

$$E_i = E_0 \epsilon^{(ik_1z-i\omega t)} \qquad H_i = \frac{k_1}{\omega\mu_1} E_i \qquad (1.1)$$

$$E_r = E_1\epsilon^{(-ik_1z-i\omega t)} \qquad H_r = \frac{-k_1}{\omega\mu_1} E_r \qquad (1.2)$$

Region 2

$$E_s = E_2^+ \epsilon^{ik_2z} + E_2^- \epsilon^{-ik_2z} \; \epsilon^{-i\omega t} \qquad (1.3)$$

$$H_s = \frac{k_2}{\omega\mu_2} \; E_2^+ \epsilon^{ik_2z} - E_2^- \epsilon^{-ik_2z} \; \epsilon^{-i\omega t} \qquad (1.4)$$

Region 3

$$E_t = E_3\epsilon^{(ik_3z-i\omega t)} \qquad H_t = \frac{k_3}{\omega\mu_3} \; E_t \qquad (1.5)$$

where normal incidence is assumed [24].

30

The propagation factor for each region is respectively,

$$k_1 = \sqrt{\omega^2 \varepsilon_1 \mu_1} \tag{1.6}$$

$$k_2 = \sqrt{\omega^2 (\varepsilon_2' + i\varepsilon_2'')\mu_2} \tag{1.7}$$

$$k_3 = k_1 \tag{1.8}$$

The entire field description is completed by determining $\bar{E}_2^+$, $\bar{E}_2^-$, and $k_2$ from the experimental values of the magnitudes of the transmission coefficient $T_0$ and reflection coefficient $R_0$, and the incident energy of the control beam. From Stratton's [9] book the transmission and reflection coefficients for an absorbing layer are respectively,

$$T_0 = \left| \frac{1}{(1+z_{12})(1+z_{23})} \frac{4\varepsilon^{i(k_2-k_3)d}}{1 + r_{12}r_{23}\varepsilon^{2ik_2d}} \right|^2 \tag{1.9}$$

$$R_0 = \left| \frac{r_{12} + r_{23}\varepsilon^{2ik_2d}}{1 + r_{12}r_{23}\varepsilon^{2ik_2d}} \right|^2 \tag{1.10}$$

where,

$$Z_{j\ell} = \frac{\mu_j k_\ell}{\mu_\ell k_j} \tag{1.11}$$

$$r_{j\ell} = \frac{1 - Z_{j\ell}}{1 + Z_{j\ell}} \qquad j,\ell = 1,2,3 \tag{1.12}$$

31
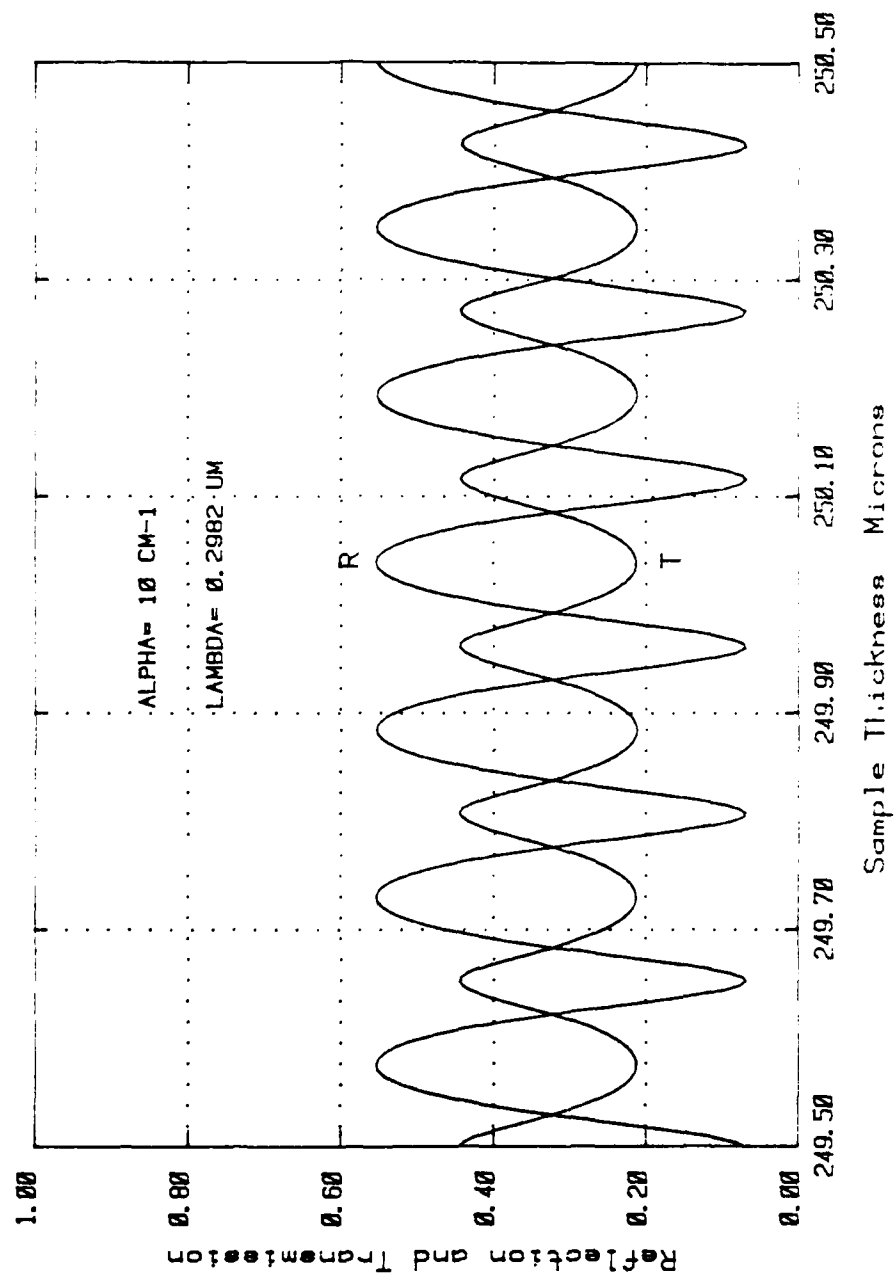
Figure 12  Reflection and transmission coefficients as a function of sample thickness.

32

and

$$k_2 = n_2 + i \kappa_2. \tag{1.13}$$

The computed values of $T_0$ and $R_0$ can be matched to their experimental values by varying $\kappa_2''$ in $k_2$. Thus $\alpha_2$, the absorption coefficient in silicon at a wavelength of 1.06$\mu$m can be found experimentally. As a result, the experimental values of the absolute values squared of $E_2^+$ and $E_2^-$ can be obtained with the knowledge of the transmission coefficient, reflection coefficient, and incident energy of the control beam. Care must be exercised when obtaining the experimental value for $\alpha_2$ when using equations (1.9) and (1.10). The expected value for silicon at the wavelength of interest (1.06 $\mu$m) is of the order of 10 cm$^{-1}$. As a consequence, a small error in the measurement of the sample thickness $d$ leads to a large uncertainty in the experimental value of $\alpha_2$. This is a direct result of the reflection and transmission expressions which are oscillating functions of the thickness $d$. Figure 12 plots equations (1.9) and (1.10) in which $\alpha_2$ has been set to 10 cm$^{-1}$.

The mean intensity of the light pulse is described by the real part of the complex Poynting vector

$$S = \mathrm{Re}\left[ \frac{1}{2} \vec{E} \times \vec{H}^* \right]. \tag{1.14}$$

Thus, the energy per unit time and unit area coupled into the semiconductor at $z = 0$ is,

$$S_0 = \mathrm{Re}\left[ \frac{1}{2} \vec{E}_s \times \vec{H}_s^* \right]. \tag{1.15}$$

33

Substituting equations (1.3) and (1.4), we obtain,

$$S_0 = \frac{\beta_2}{2\omega\mu_2} \left( |E_2^+|^2 - |E_2^-|^2 \right) \tag{1.16}$$

and,

$$S_0 = S_i(1-R_0) \tag{1.17}$$

where $S_i$ is the incident energy per unit time and unit area and $R_0$ is the reflection coefficient.

The energy of the control beam at $z = d$ can be expressed as,

$$S_d = \frac{\beta_2}{2\omega\mu_2} \left( |E_2^+|^2 \, \varepsilon^{-2\alpha_2 d} - |E_2^-|^2 \, \varepsilon^{2\alpha_2 d} \right) \tag{1.18}$$

where $\alpha_2$ is the absorption coefficient. As a result, the total energy per unit time and unit area lost within the semiconductor is,

$$S_a = S_0 - S_d \,. \tag{1.19}$$

Substituting equations (1.16) and (1.18) into (1.19) we obtain,

$$S_a = \frac{\beta_2}{2\omega\mu_2} \left( |E_2^+|^2 \, (1-\varepsilon^{-2\alpha_2 d}) - |E_2^-|^2 \, (1-\varepsilon^{2\alpha_2 d}) \right) \tag{1.20}$$

which can also be stated as,

$$S_a = S_i (1 - R_0 - T_0) \tag{1.21}$$

where $R_0$ and $T_0$ are the reflection and transmission coefficients respectively.

Equations (1.16) and (1.20) can be equated to equations (1.17) and (1.21) respectively to form two simultaneous equations where $|E_2^+|^2$ and $|E_2^-|^2$ can be determined. The results are,

34

$$|E_2^+|^2 = S_i \frac{(1-R_0)\,\varepsilon^{2\alpha_2 d} - T_0}{\frac{\beta_2}{2\omega\mu_2}\{\varepsilon^{2\alpha_2 d} - \varepsilon^{-2\alpha_2 d}\}} \tag{1.22}$$

$$|E_2^-|^2 = S_i \frac{(1-R_0)\,\varepsilon^{-2\alpha_2 d} - T_0}{\frac{\beta_2}{2\omega\mu_2}\{\varepsilon^{2\alpha_2 d} - \varepsilon^{-2\alpha_2 d}\}} \tag{1.23}$$

Finally, the electron-hole distribution per unit time and unit volume at $t = 0$ needs to be determined. Taking the real part of the divergence of the Poynting vector within the semiconductor gives the energy absorbed per unit time and unit volume as a function of $z$. Thus,

$$\varsigma(z) = Re\left(\frac{1}{2}\vec{E}_s \times \vec{H}_s^*\right) \tag{1.24}$$

substituting equations (1.3) and (1.4) into (1.24) and differentiating, we obtain,

$$\varsigma(z) = -\frac{\alpha_2\beta_2}{\omega\mu_2}\left[|E_2^+|^2\,\varepsilon^{-\alpha_2 z} + |E_2^-|^2\,\varepsilon^{2\alpha_2 z}\right]. \tag{1.25}$$

If we assume that one electron-hole pair is generated with the absorption of one photon of wavelength equal to 1.06 µm for low carrier levels, then equation (1.25) can be set equal to $-C(z)\hbar\omega$ where $C(z)$ is the concentration of the carriers per unit time and unit volume and $\hbar\omega$ is the energy of one photon. Thus,

$$C(z) = \frac{\beta_2\alpha_2}{\omega^2\mu_2\hbar}\{|E_2^+|^2\,\varepsilon^{-2\alpha_2 z} + |E_2^-|^2\,\varepsilon^{2\alpha_2 z}\} \tag{1.26}$$

where $|E_2^+|$, $|E_2^-|$, and $\alpha_2$ are determined from experimental data.

35

B. CARRIER REDISTRIBUTION

Once the short burst of energy passes through the silicon crystal
at time equal to 0+, the photo-excited electron-hole pairs will diffuse to
less populated areas. In addition, the electrons and holes will recom-
bine with each other with a characteristic lifetime. This annihilation
process will reduce the total number of pairs as time progresses. The
continuity equations that describe this process are,

$$\frac{\delta n}{\delta t} = -R_n + \mu_n \nabla \cdot (n\vec{E}) + D_n \nabla^2 n \qquad (1.27)$$

$$\frac{\delta p}{\delta t} = -R_p + \mu_p \nabla \cdot (p\vec{E}) - D_p \nabla^2 p \qquad (1.28)$$

for electrons and holes respectively.

Equations (1.27) and (1.28) can be combined into one single equa-
tion that describes the motion of electrons and holes within the semicon-
ductor. Several assumptions have to be made to obtain such equations.
The optically excited electron and hole concentrations $n'$ and $p'$ are
assumed equal throughout the crystal. As a result, the difference between
the total electron and hole density, $n$ and $p$ respectively, is very small.
In addition, their time and space derivatives are assumed to be equal. In
reality, however, as the electrons and holes redistribute, the electrons
tend to diffuse faster than the holes since the electrons have a larger
diffusion coefficient than the holes ($D_n > D_p$). As a consequence, an
electric field develops between the electrons and holes as their imbalance
increases. Thus, the hole diffusion is aided by this field while the
electron diffusion is slowed down. The basic assumption states that
although the electron and hole diffusion coefficients are different, the
electric field from charge unbalance prevents the excited carriers'

concentrations and their respective derivatives from differing signifi-

cantly from each other throughout the semiconductor. As a result, a sim-

ple diffusion equation with its corresponding "ambipolar" mobility $\mu_a$,

lifetime $\tau_a$, and diffusion coefficient $D_a$, may be used [25].

By multiplying equation (1.27) by $\mu_p p$ and equation (1.28) by $\mu_n n$,

adding the resulting two equations and assuming

$$\frac{\delta p}{\delta t} = \frac{\delta n}{\delta t} \tag{1.29}$$

$$p = n \tag{1.31}$$

$$\nabla^2 p = \nabla^2 n \tag{1.32}$$

and using Einstein's Relationship $D = \frac{kT}{q\mu}$ to obtain

$$D p \mu_n = D n \mu_p$$

we may finally write,

$$\frac{\delta n}{\delta t} \mu_p p + \mu_n n = -R_n \mu_p p - R_p \mu_n n - \mu_n \mu_p (p-n) \vec{E} \cdot \nabla n$$
$$+ \mu_p D n (n+p) \nabla^2 n \tag{1.33}$$

The electron and hole recombination rates $R_n$ and $R_p$ respectively, are

assumed to be linear. That is,

$$R_n = \frac{n'}{\tau_n} \tag{1.34}$$

and

$$R_p = \frac{p'}{\tau_p} \tag{1.35}$$

where $n'$ and $p'$ are the optically excited electrons and holes. Thus the

total carrier densities n and p are equal to a background level $n_0$ and $p_0$

summed to an excited level $n'$ and $p'$ respectively. That is, $n = n' + n_0$

37

and $p = p' + p_0$. By dividing equation (1.33) by $(\mu_n n + \mu_p p)$ and substituting equations (1.34) and (1.35) we finally obtain the "ambipolar" diffusion equation

$$\frac{\delta n'}{\delta t} = \frac{-n'}{\tau_a} + \mu_a \vec{E} \cdot \nabla n' + D_a \nabla^2 n' \tag{1.36}$$

where $\tau_a$, $\mu_a$, and $D_a$ are the ambipolar lifetime, mobility, and diffusion coefficient, respectively;

$$\tau_a = \frac{\mu_p p + \mu_n n}{\dfrac{\mu_p p}{\tau_n} + \dfrac{\mu_n n}{\tau_p}} \tag{1.37}$$

$$\mu_a = \frac{p - n}{\dfrac{n}{\mu_p} + \dfrac{p}{\mu_n}} \tag{1.38}$$

and,

$$D_a = \frac{p + n}{\dfrac{n}{D_p} + \dfrac{p}{D_n}} \tag{1.39}$$

The electric field $\vec{E}$ within the semiconductor due to the charge imbalance can be ignored [25]. In addition, since $n'$ is approximately equal to $p'$, $p-n$ is very small leading to a very small value for the ambipolar mobility $\mu_a$. As a result, the second term on the right side of equation (1.36) can be considered as second order in comparison to the others. We may write the ambipolar diffusion equation as,

$$\frac{\delta n'}{\delta t} = \frac{-n'}{\tau_a} + D_a \nabla^2 n' \tag{1.40}$$

38
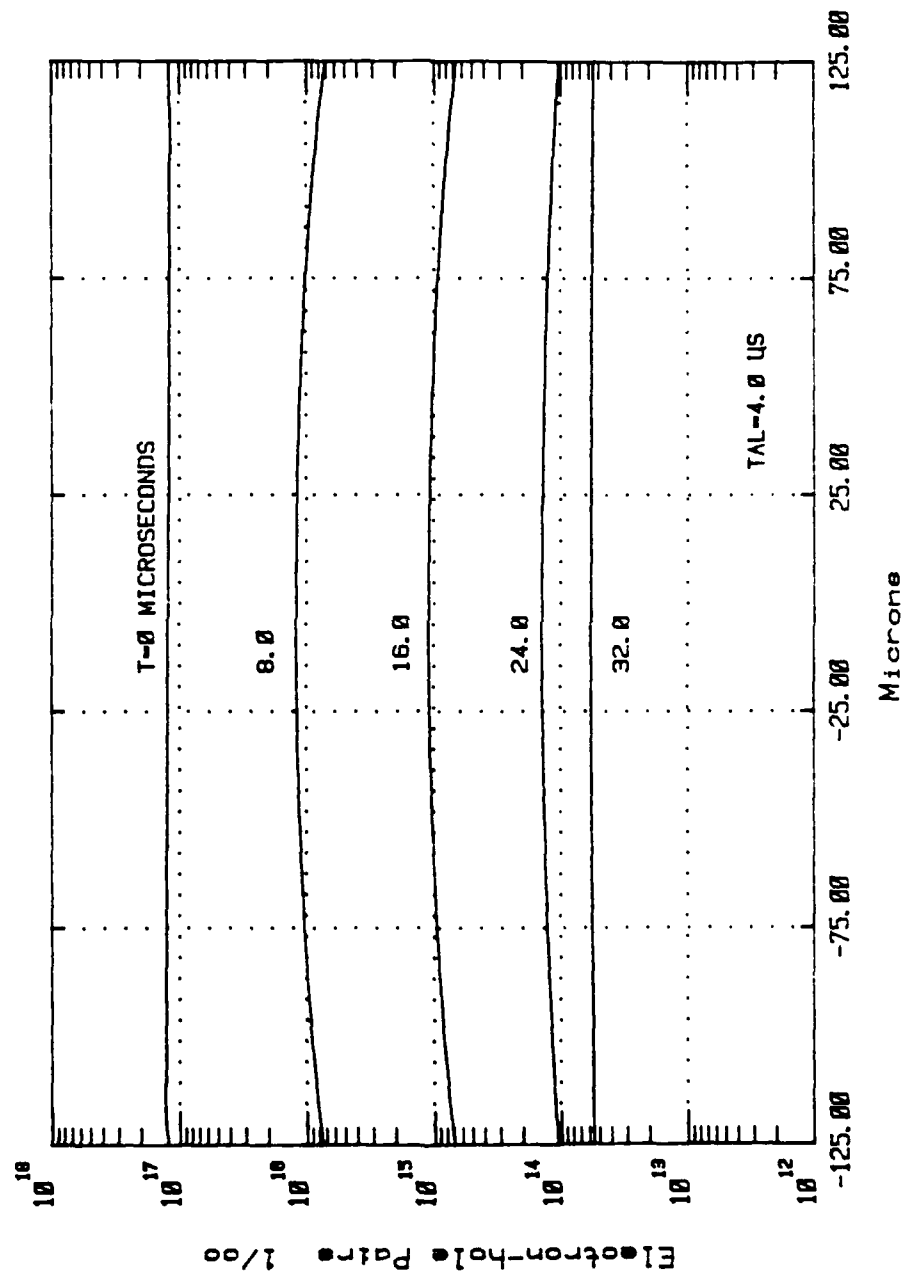
Figure 13   Spatial distribution and time decay of excess carriers.

39

A solution to the above differential equation in one dimension , may be formed by a linear superposition of solutions of the form [26],

$$n'(z,t) = \sum_{k=0}^{\infty} (A_k \cos C_k Z + B_k \sin c C_k Z) \varepsilon^{-\nu_k t} \qquad (1.41)$$

where

$$\nu_k = \frac{1}{\tau_a} + DaC_k^2. \qquad (1.42)$$

The coefficients $A_k$, $B_k$, and $C_k$ must be chosen to satisfy the initial condition (see equation 1.26),

$$n'(z,t=0) = \frac{\beta 2\alpha 2}{\omega^2 \mu 2h} |E_2^+|^2 \varepsilon^{-2\alpha 2z} + |E_2^-|^2 \varepsilon^{2\alpha 2z} \qquad (1.43)$$

and the boundary conditions,

$$\pm Da \left. \frac{\delta n'}{\delta z} \right|_{z=\mp d} = sn' \qquad (1.44)$$

where s is the surface recombination velocity at the two boundaries depicted by $z = \pm d$. That is, the thickness of the semiconductor slab is equal to 2d.

A complete derivation of equations (1.41) and (1.42) is presented in Appendix 4. Figure 13 is a plot of equation (1.41) for an arbitrary input energy and an ambipolar lifetime of 4.0 microseconds. It should be pointed out that the reduction of carrier density at the sample's surfaces is due to surface recombination. Here a worst case value of 1000 centimeters per second is chosen for a silicon wafer 250 micrometers thick. The time increments depicted in Figure 13 are equal to 8 microseconds.

As a final note in this section, the mobilities of electrons and holes are not assumed to be constant. As a matter of fact they are

40

functions of the number of impurity atoms within the crystal, lattice temperature, and the excess carriers [27]. As a result, the ambipolar diffusion coefficient will vary as the number of electron-hole pairs decays. A complete formulation to obtain these parameters is included in Appendix B.

## C.  INFRARED ABSORPTION

In this section a theory will be presented which describes the
absorption of light having a wavelength near ten microns.  The absorption
of radiation energy can be expressed as the exponential decay of the
photon flux with distance inside the semiconductor.  We may write [28]

$$I_{out} = I_{in} \varepsilon^{-\alpha D} \tag{1.45}$$

where $I_{in}$ and $I_{out}$ are the input and output intensities of the ten micron
light, $\alpha$ the absorption coefficient, and D is the sample thickness.  Note
that equation (1.45) neglects the fact that part of the incident light is
reflected at the first surface where it enters the sample, and that
another part is reflected back into the sample at the second surface
where the light exists.  Equation (1.45) can be satisfied by placing
the silicon wafer at the Brewster's angle for the $10\mu m$ radiation.

There are several absorption mechanisms occuring in silicon for
radiation near ten microns.  Light will be absorbed by the creation of
phonons within the lattice of the semiconductor [29].  The effect of
lattice absorption depends on the wavelength of the light and the
temperature of the material.  In addition, absorption due to free
electrons is also possible although the cross section for this process is
much smaller than for other absorption mechanisms.  Finally, the mechanism
in which a free-hole absorbs a photon by making a direct intravalence band
transition is also included.  These direct transitions include heavy-hole
to light-hole band transition, heavy-hole to split-off band transition,
and light-hole to split-off band transition [30].

42

As a result, we may write the absorption coefficient for silicon for ten micron radiation as,

$$\alpha = \alpha_p + \alpha_{h \to \ell} + \alpha_{h \to s} + \alpha_{\ell \to s} + \alpha_f \tag{1.46}$$

where $\alpha_p$ is the absorption due to phonons, the following three terms are the absorption due to the direct intravalence band transitions, and $\alpha_f$ is the absorption due to free carriers. The three intravalance band transition coefficients can be grouped into one absorption term $\alpha_d$. In addition, if $\sigma_d$ and $\sigma_f$ represent the hole and free-carrier radiation absorption cross section respectively, we may write,

$$\alpha = \alpha_p + \sigma_d p + \sigma_f n \tag{1.47}$$

where n and p are the electron and hole densities. As a result, the transmission coefficient of the probing beam can be rewritten as,

$$T = e^{-(\sigma_d p + \sigma_f n)D} \tag{1.48}$$

where static effects such as lattice absorption and any hole contribution from doping atoms have been subtracted out.

The expression that relates the free carrier absorption coefficient to the density of electrons within a semiconductor results from classical dispersion theory. The absorption increases as the square of the wavelength $\lambda$ and is directly proportional to the carrier density n. We may write [28]

$$\alpha_f = \frac{\lambda^2 Q^3}{4\pi^2 C^3 n_r \varepsilon_0} \frac{n}{m_n^2 \mu_n} \tag{1.49}$$

where Q is the electron charge, C is the speed of light, $n_r$ is the

refractive index, $\varepsilon_0$ is the vacuum permittivity, $m_n$ is the electron mass, and $\mu_n$ is the electron mobility. This absorption is due to the absorption of light when a free electron is raised to a new energy state.

The direct intravalence-band transition can be described as the absorption of light when a bound electron is excited to a higher energy state within the three sub-bands in the valence band. Both energy and momentum are conserved in the intravalence band transitions. As a result, only holes in a narrow region of the heavy and light hole bands will contribute in the absorption of 10 μm light [31]. The absorption coefficient is governed by the populations of these sub-bands which are present when an electron-hole pair is generated by 1.06 μm light. The hole states involved in the optical transition are maintained close to the dynamic value by various scattering processes of which the dominant is hole-phonon relaxation [32]. This scattering rate occurs with a sub-picosecond time constant.

The expression relating the absorption coefficient as a function of available holes on the valence sub-bands results from a quantum mechanical treatment of the transitions. The resulting form for $\alpha_d$ is [31,32],

$$\alpha_d = \frac{4\pi Q^2 p}{n_r C m_p} \frac{\tau}{1 + \tau^2 \omega^2} \tag{1.50}$$

where $\tau$ and $p$ are the relaxation time and density of holes respectively, and $\omega$ is the angular frequency of the incident radiation.

In addition to the aforementioned processes, a dynamic lattice absorption is possible in silicon. Two-phonon absorption is energet-
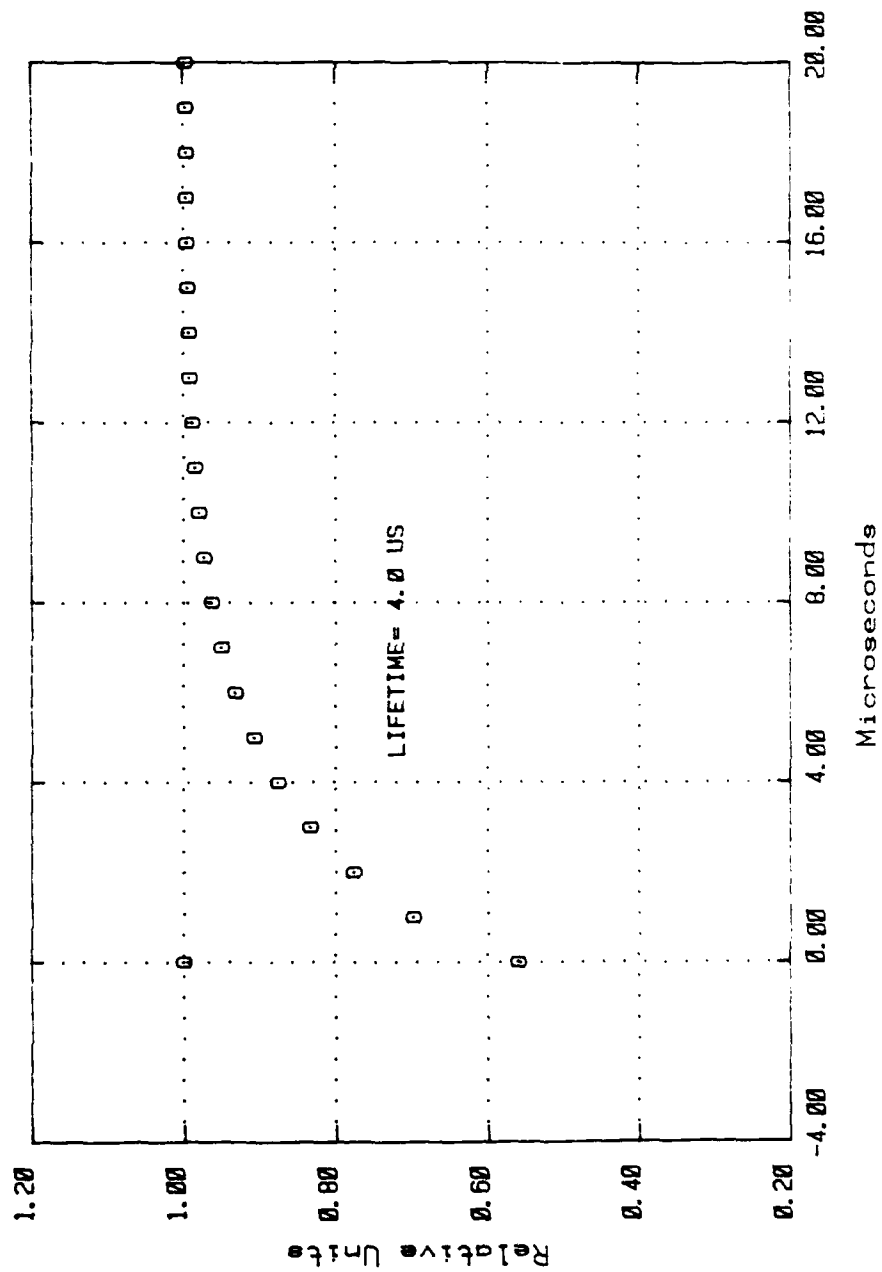
44

Figure 14 Time-dependence of modulated $CO_2$ laser beam. Carrier lifetime is 4.0 microseconds.

45

ically possible for a wavelength of 10.6 microns [32]. The probability
of occurrence is increased dramatically since phonons are generated when
a free-electron recombines with a hole during the decay process.
Furthermore, indirect free-hole transitions are possible where an elect-
ron is excited within the same band with simultaneous generation or
absorption of a phonon [34]. This process follows the same dependence as
the free-electron absorption does where $\alpha$ increases as a function of $\lambda^2$.
As a consequence of these added absorption processes, the hole cross-
section $\sigma_d$ in silicon is expected to be slightly larger than quoted in
the literature [31].

Equation (1.48) is plotted as a function of time in Figure 14.
The electron and hole concentrations are determined using equation (1.41)
with the same boundary conditions utilized to plot Figure 13. Note that
since the level of photo-excited carriers is non-uniform, an iterative
method with a 1 micrometer space increment is implemented to obtain the
normalized transmission of the 10 um light. This formulation assumes
instantaneous generation of electron-hole pairs. As a result, the rise-
time of the attenuated beam is close to zero.

Figures 15a and 15b show the energy band diagram of silicon
when optically induced transitions are include [18,20]. The 1.06um light
generates inter-band transitions whereas the 10.59 um light contributes to
intravalence band transitions. Note that bound electrons can be excited
from the top of the three valence bands at $k = 0$. This is due to the
small energy separation between the split-off band and the heavy or
light-hole bands. As a result, 1.164 electron-volts (eV) are required to
excite an electron from the top of the split-off band to the conduction
band. A 1.06 um photon has an energy of 1.172eV.

46
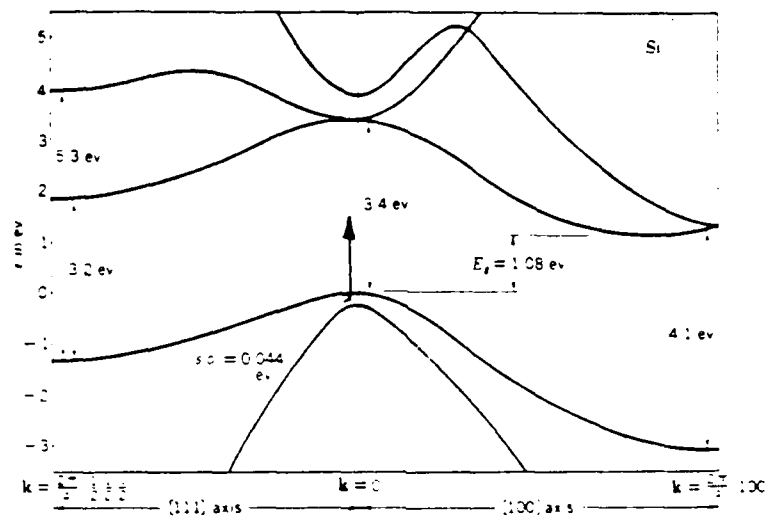
a. Interband transition (1.06 μm)
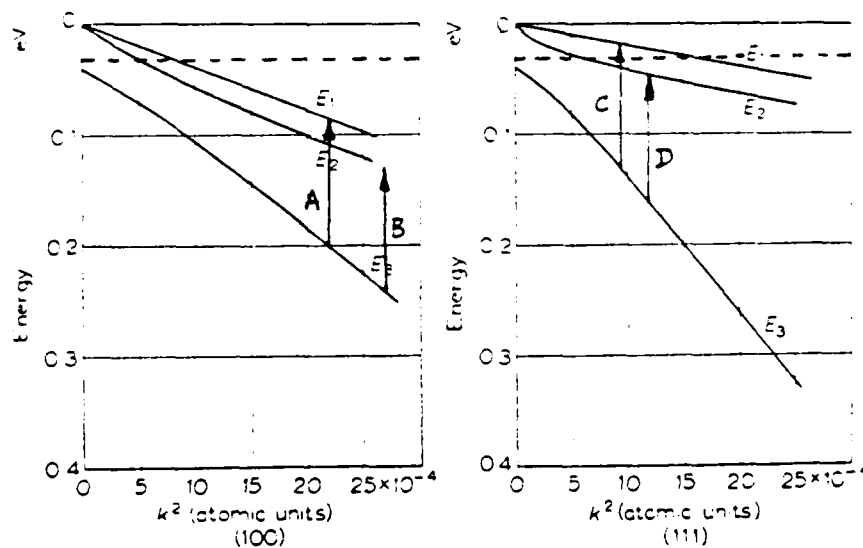


b. Intravalence band transitions (10.59 μm)

Figure 15    Silicon energy band diagram with allowed optical
transitions [18,20].

47

According to Figure 15, direct transitions are possible only between the split-off band and either the heavy or light hole band for 10.59 μm photons. The thermal energy kT at room temperature allows the population of holes on top of the heavy and light hole bands to redistribute itself. As a result transitions C and D have a much larger probability of occurence than A and B for 10.59 μm light.

T= 4C. 2 NS
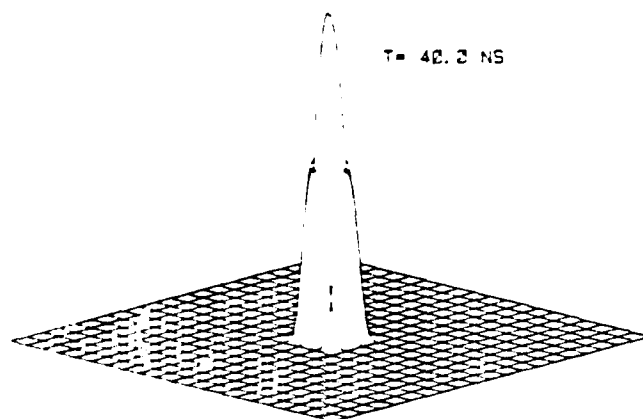
T= 1. 2 .S
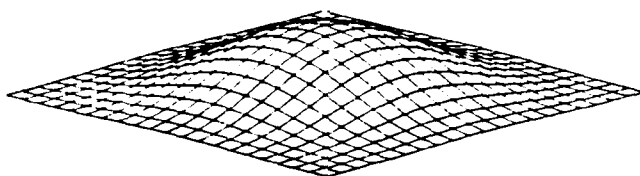
T= 2. 2 .S
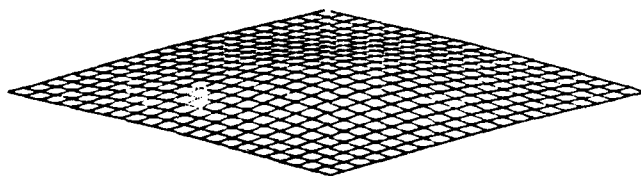
Figure 16   Carrier redistribution normal to the
            z-direction.  Lifetime is 1.0 micro-
            second, grid size is 15 x 15 $\mu$m$^2$.

T= 40.0 NS

T= 100 NS

T= 200 NS
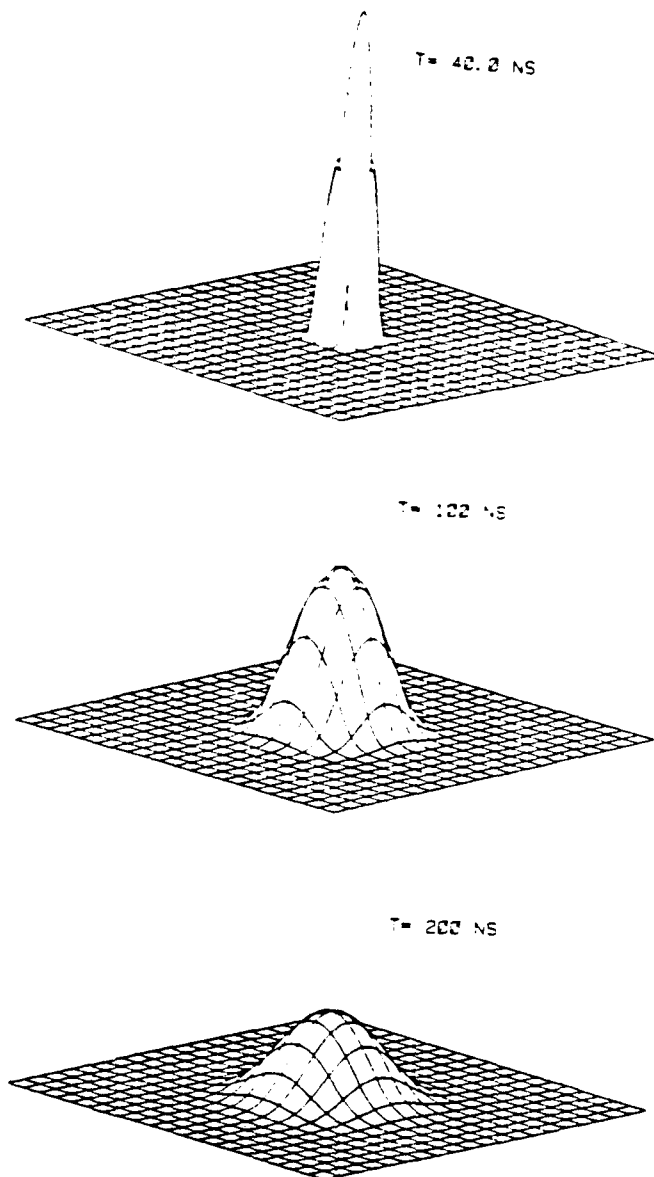
Figure 17    Carrier redistribution normal to the
z-direction.  Lifetime is 100 nano-
seconds, grid size is 15 x 15 $\mu m^2$.

50

D. CARRIER REDISTRIBUTION NORMAL TO THE DIRECTION OF LIGHT PROPAGATION

In addition to carrier decay in the z-direction, the optically
excited electron-hole pairs will diffuse outward from the area of excita-
tion. This, of course, leads to a three-dimensional picture of carrier
generation and decay within the sample. Equation (1.40) can be extended
into three dimensions resulting in

$$\frac{\delta n'(r)}{\delta t} = \frac{-n'(r)}{\tau_a} - D_a \, \nabla^2 \cdot n'(r) \tag{1.50}$$

where

$$\vec{r} = x\,\hat{a}_x + y\,\hat{a}_y + z\,\hat{a}_z \,. \tag{1.51}$$

A two-dimensional solution for equation (1.50) valid for $t > t_p$ can
be written as [11,28].

$$n'(x,y,t) = \frac{N\,t_p}{\pi t} \, \varepsilon^{-\frac{x^2 + y^2}{4D_a t} - \frac{t}{\tau_a}} \tag{1.52}$$

where N electron-hole pairs are generated instantaneously at a point
$x = y = 0$ and time = 0, $t_p$ is the finite pulse width of the exciting
laser, and $n_0$ represents the background level of free carriers. The
solution is plotted in Figure 16  for an ambipolar lifetime of 1.0 micro-
second, laser pulse width of 40 nanoseconds and 300 microjoule energy.
According to the figure, a time dependent 'smearing' of the incident laser
spot is apparent. As a result, the resolution of an infrared spatial
light modulator is dictated by material lifetime and mobility. A resolu-
tion of 4 lines per millimeter is possible where the grid size is 15 x 15
microns squared. Figure 17  demonstrates considerable improvement for a
tenfold decrease in carrier lifetime. As a result, a material with a 100
nanosecond lifetime might have a worst case resolution in the order of 8
lines per millimeter.

51

## 3. EXPERIMENTAL STUDIES

Following the theoretical analysis of Faraday rotation in semiconductors (section 2.3) it was decided to use InSb for the experimental studies rather than GaAs. Samples of bulk material were obtained and wafers were prepared. Special attention was given to characterizing samples. Data obtained included optical absorption coefficient at 1.06 micrometers, minority carrier lifetime, surface recombination velocity, electron mobility and mobility ratio. The measurement techniques used included Hall measurements, transverse magneto resistance measurements, photoconductivity and photoelectromagnetic measurements.* Since the program terminated before device studies could be made the details of the measurements will not be included here.

The basic experimental configuration where one laser controls the intensity of another laser via a semiconductor crystal requires that the two light sources be coincident within the sample. Few mirrors and lenses are used to direct and focus both laser beams resulting in a very simple experimental layout.

This chapter is organized in the following way: in Part 3.1 a description of the lasers used and their respective detectors is presented; in Part 3.2 instrumentation and circuitry utilized in the experiment are described; in Part 3.3 the results of this work are presented and correlated with theoretical results. A step by step procedure is also included in Part 3.3 for using some experimental results to obtain sample constants using theoretical formulations; in Part 3.4 the improved switching time of a gold diffused sample is presented; in Part 3.5 a description of the experimental layout to obtain a rough estimate of the infrared modulator's spatial resolution is shown.

---

* Min, Wi-sik, Steady State Excess Carrier Distribution in n-Type InSb under Illumination by Light, M.S. Thesis, Ohio State University, 1981.
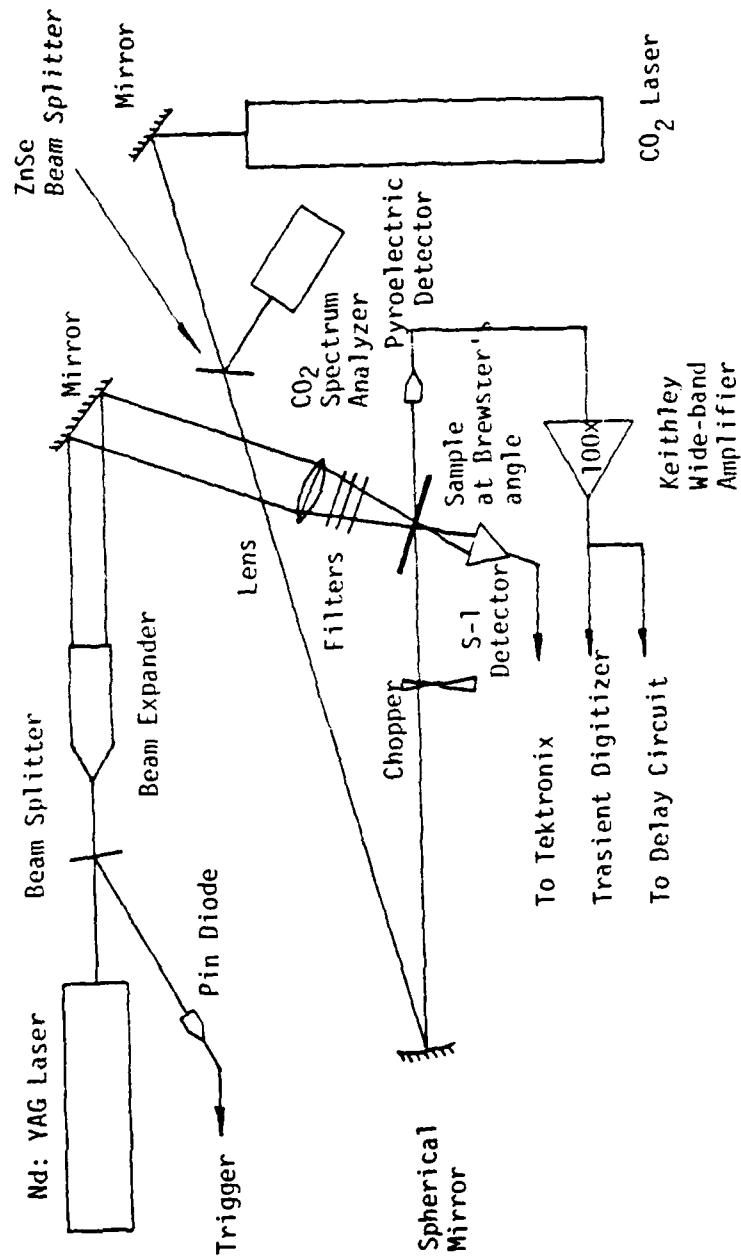
Figure 18    Experimental layout for an optical light modulator.

0.02 volts/div.          50000 nanosec/div.
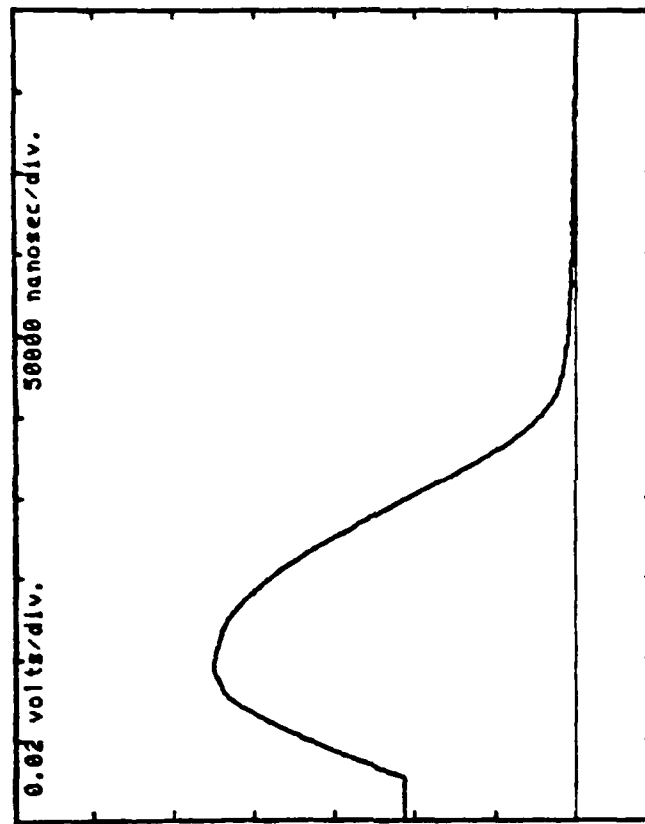
Figure 19   Chopped $CO_2$ laser light waveform.

## 3.1   APPARATUS DESCRIPTION

Figure 18 shows the experimental layout where the sample, a silicon wafer polished on both sides, is shown at the center. The output from the pulsed Nd:YAG laser, positioned at the top of the figure is expanded into a two inch beam which is directed onto the back side of the sample for normal incidence by a mirror. Neutral density filters are placed on its path to obtain several power levels. A lens is utilized to insure that the 1.06 $\mu$m radiation completely overlaps the 10.59 $\mu$m radiation. An iris in place of the sample is used to align both beams. An RCA S-1 vacuum diode positioned in front of the sample monitors the control beam's incident and transmitted powers. Finally, a beam splitter positioned at the output of the Nd:YAG laser provides a trigger signal through a Centronic BPX 65 detector with a 1 nanosecond risetime.

An International Laser Systems (ILS) Q-switched Neodymium: Yttrium Aluminum Garnet (Nd:YAG) laser with a wavelength of 1.06 $\mu$m is used as the control beam. The 40 nanosecond pulse provided by the ILS laser has an average peak power of 7.5 kilo watts. The probing infrared beam is provided by a modified MPB Technologies carbon-dioxide ($CO_2$) laser operating at a wavelength of 10.59 $\mu$m. The $CO_2$ mixture (10% $CO_2$, 10% Nitrogen, balance Helium) is supplied to the continuous wave (CW) laser cavity utilizing an open flow system.

The signal beam, the 10.59 $\mu$m radiation, is provided by a chopped $CO_2$ laser positioned on the far right in Figure 19. This beam is directed and focused to a spot 1 millimeter in diameter on the left hand side of the

Figure 20   Delay circuit utilized to synchronize the two lasers
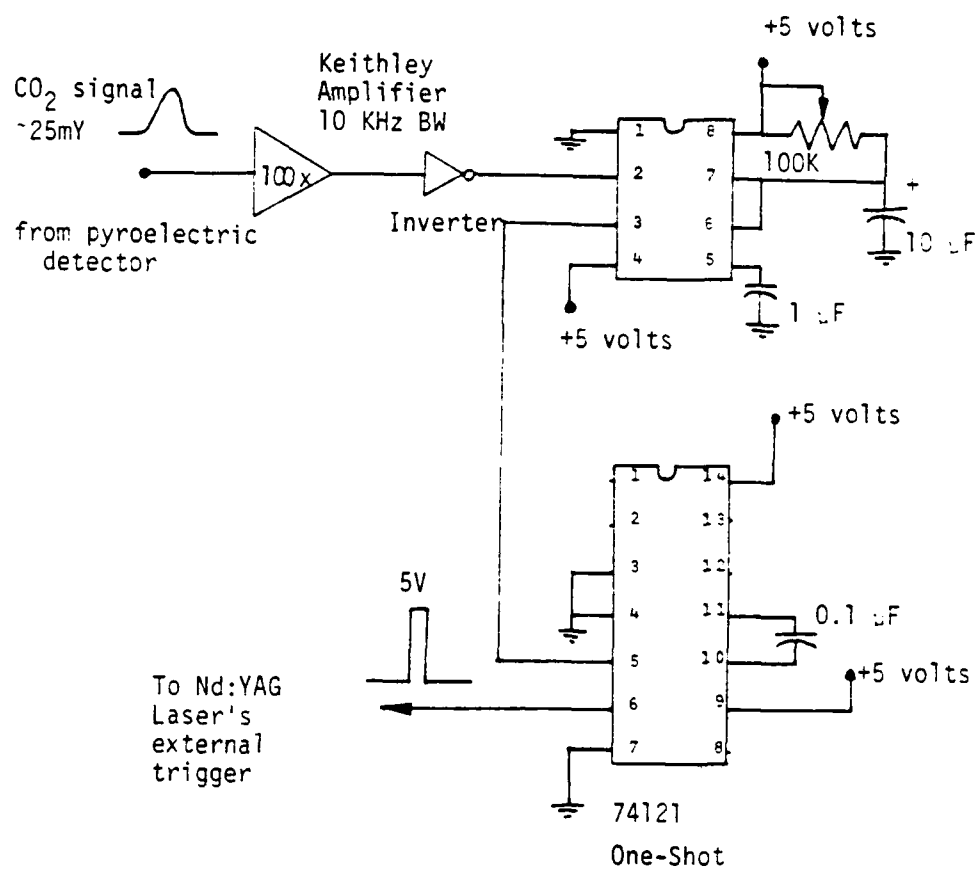with the proper time delay.

sample with parabolic and flat surface mirrors. The parabolic mirror is of relative large focal length to avoid any significant focusing as the beam propagates through the sample. The sample is positioned at the Brewster's angle to remove any contributions to the observed material effect from the reflection due to the and second surfaces. The wavelength of the $CO_2$ laser is continuously monitored by an infrared spectrum analyzer and Zinc-Selenide (ZnSe) beam splitter positioned at the output of the laser. Finally, a pyroelectric detector with a 60 nanosecond risetime Field-Effect transistor preamplifier is used to measure the time-dependence of the modulated 10.59 μm radiation.

The Nd:YAG laser is pulsed at a rate of 1 Hertz to obtain a stability within 10% from shot to shot. A delay circuit is required to synchronize the two lasers with the proper time delay. As a result, the simultaneous occurrence of both lasers within the sample is insured. Figure 19 shows the chopped 10.59 um radiation which consists of a train of 250 microsecond pulses at a frequency of 25 hertz. This signal is amplified 10,000 times through a low-pass filter and fed into a delay circuit depicted in Figure 20. Consquently, the required 1 Hertz trigger pulse is generated by the $CO_2$ laser's output.

## 3.2  DATA COLLECTION AND INSTRUMENTATION

A Tektronix digitizer with its controlling microcomputer with graphics capabilities is used for all data collection and storing. In addition, waveform integration and differentiation are possible through numerical methods.

Since the pulse energy of the Nd:YAG laser is highly reproducible from shot to shot, the incident energy on the sample is separately

TABLE 3.1   INSTRUMENTATION

### LASERS

| Type | $t_p$(measured) | Power(measured) | $\lambda$ |
|------|-----------------|-----------------|-----------|
| CO2  CW | 250 µs chopped | 2 W | 10.59 µm |
| ND:YAG | 40  ns | 7.5 KW | 1.06 µm |

### DETECTORS

| Type | $t_r$ | Responsivity @ $\lambda$ |
|------|-------|--------------------------|
| pyroelectric | 60 ns FET pre-amp | 0.37 mV/w @ 10.59 µm |
| S-1 diode | 150 ps | 20.0 mV/w @ 1.06 µm |
| PIN diode | 1 ns (50Ω) | - |

### AMPLIFIERS

| Type | BW | Purpose |
|------|-----|---------|
| Keithley 100X | 100 MHz (50Ω) | raise signal level |
| Keithley 100X | 10 KHz | raise signal level for delay circuit |

### DIGITIZER

| | |
|---|---|
| Tektronix   7912AD | 500 MHz (50Ω) |
| Tektronix   4051/4631 | Micro computer/copier |

Step 1      Incident.reflection, and transmitted 1.06 micron energies

Step 2      Absorption coefficients at 1.06 microns

Step 3      Magnitudes of electric fields squared at 1.06 microns
            within the semiconductor

Step 4      Time and spatial distribution of optically generated
            carriers

Step 5      Average hole cross section at 10.59 microns

Step 6      Modulated time-dependent $CO_2$ laser beam

Figure  21   Sequential steps followed for data
             collection and computation

INCIDENT AND REFLECTED 1.06 RADIATION IN SILICON

20 nanosec/div.

1 volts/div.
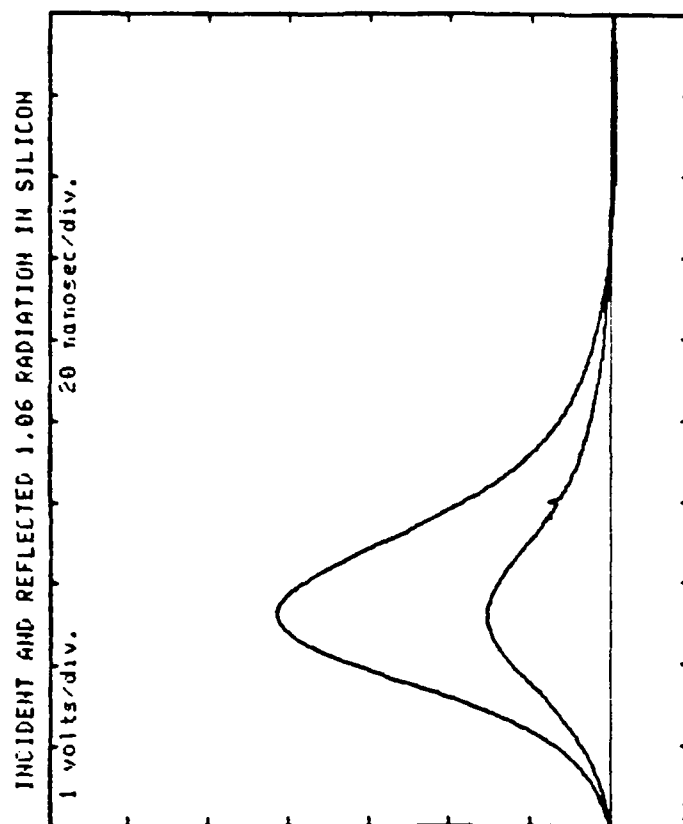
a. Reflected energy R = 0.1548

Figure 22a Experimental curves for incident and reflected 1.06 μm light pulses normal to a silicon wafer.

INCIDENT AND TRANSMITTED 1.06 RADIATION IN SILICON

1 volts/div.

20 nanosec/div.
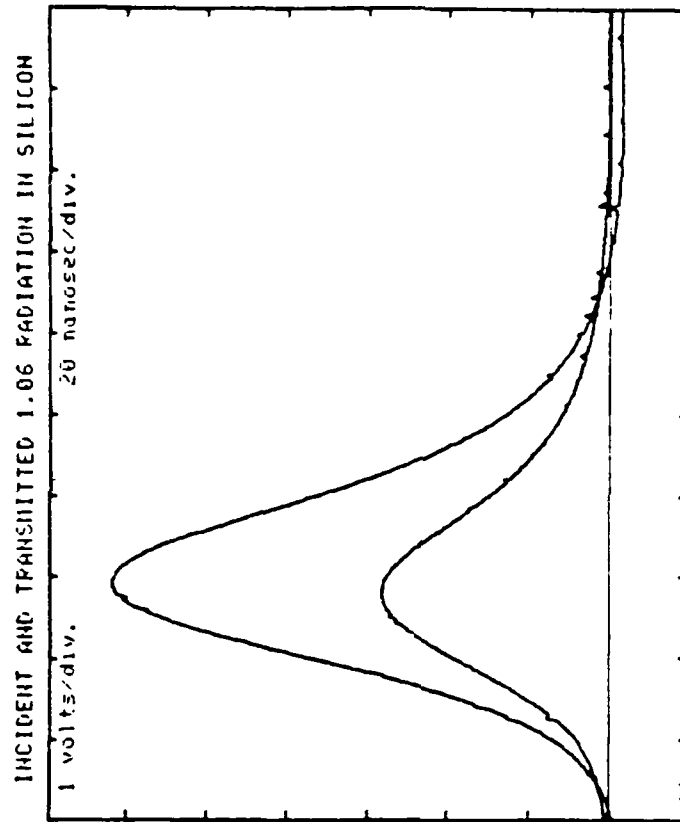
b. Transmitted energy T = 0.4214

Figure 22b    Experimental curves for incident and transmitted 1.06 μm light pulses normal to a silicon wafer.

Control Laser Energy Microjoules
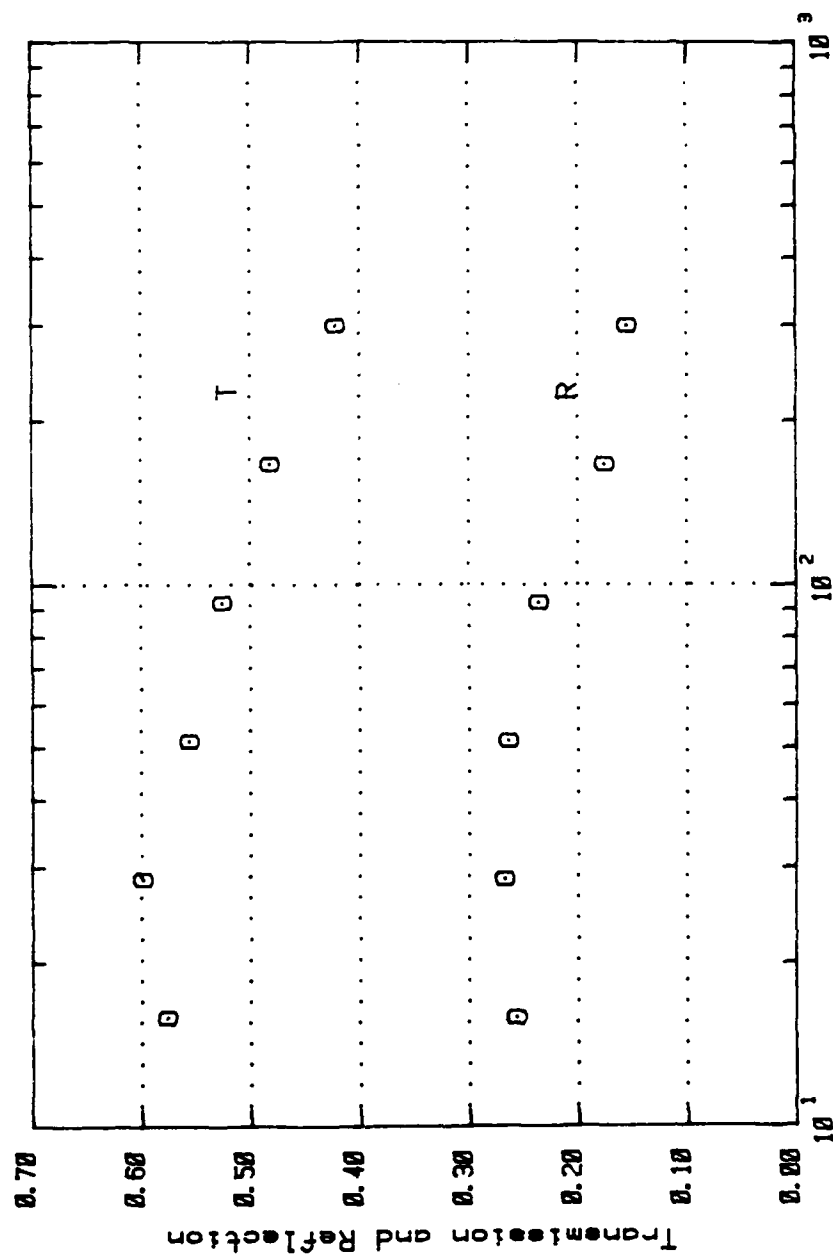
Figure 23    Experimental reflection and transmission coefficients in silicon as a function of 1.06 μm light energy.

62

Figure 24    Calculated absorption coefficient in silicon as a function of 1.06 μm
            light energy.

63

measured from the transmitted energy by simply removing the sample. These energies are computed by integrating the laser pulse waveform.

The intensity and baseline of the $CO_2$ laser beam is continuously monitored by chopping the laser's output. Because of the low responsivity of the pyroelectric detector, a Keithley wideband amplifier with a gain of 100 times is utilized. This signal 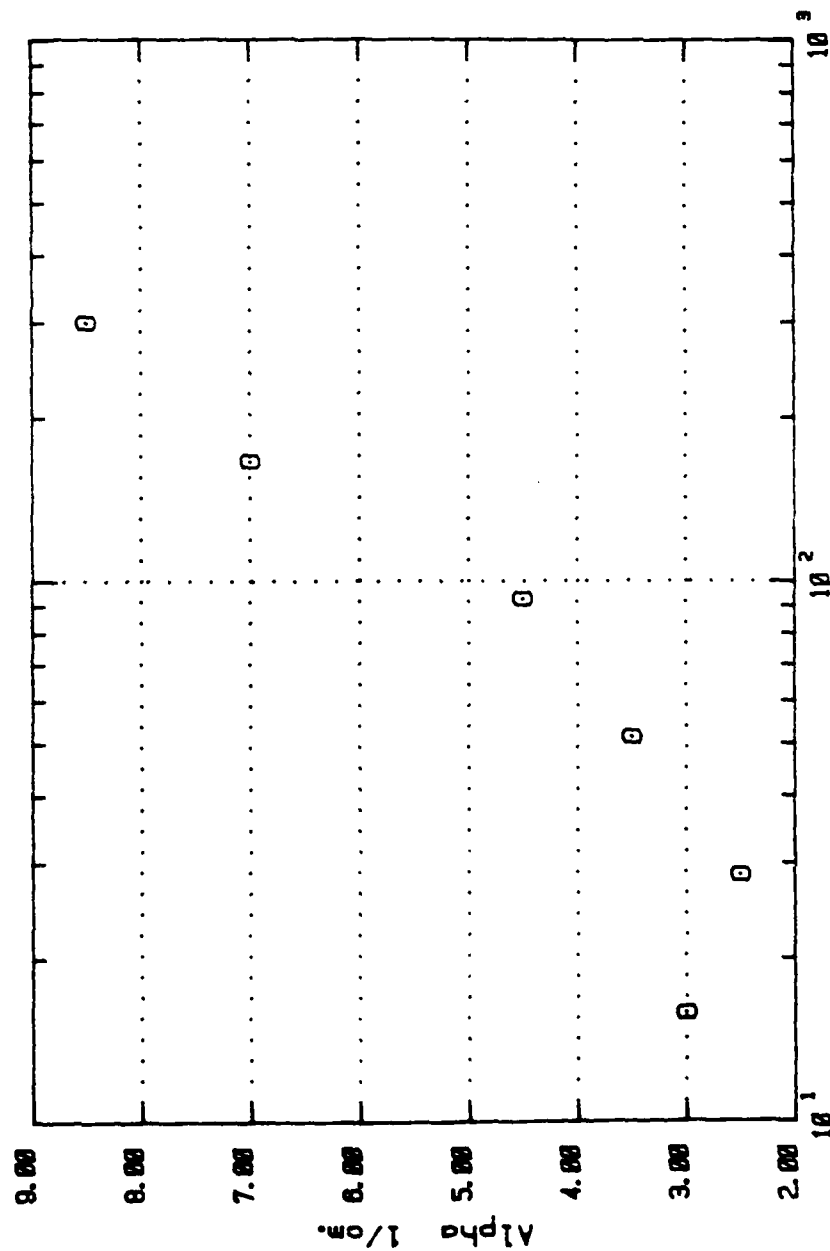is fed into the digitizer triggered by the PIN diode sampling the output of the Nd:YAG laser. As a result, the digitizer displays only a 10.59 μm signal when a 1.06 μm pulse is present.

Table 3.1 summarizes all pertinent data corresponding to lasers, detectors, and instrumentation.

## 3.3 PRESENTATION OF DATA AND CORRELATION WITH THEORETICAL RESULTS

A silicon wafer polished on both surfaces with a thickness of 250 microns is used as a sample in this experiment. The material is p-type with resistivity of 500 ohm-centimeter corresponding to a doping density of $2x10^{13}$ Boron atoms per cubic centimeter.

Experimentally, three sets of data are generated. The order of events as depicted in Figure 21 is as follows: Incident, reflected and transmitted energies of 1.06 μm are measured from which experimental reflection and transmission coefficient result. Figures 22a and 22b show the resulting averaged Nd:YAG laser waveforms for one power level. By using equations (1.9) through (1.13) a value for $\alpha$, the absorption coefficient in silicon at 1.06 microns is obtained. The resulting coefficients are shown in Figures 23 and 24 as a function of incident energies. Note that close to 25% of the incident radiation is reflected. An antireflective coating provided by a thermally grown film of silicon

64
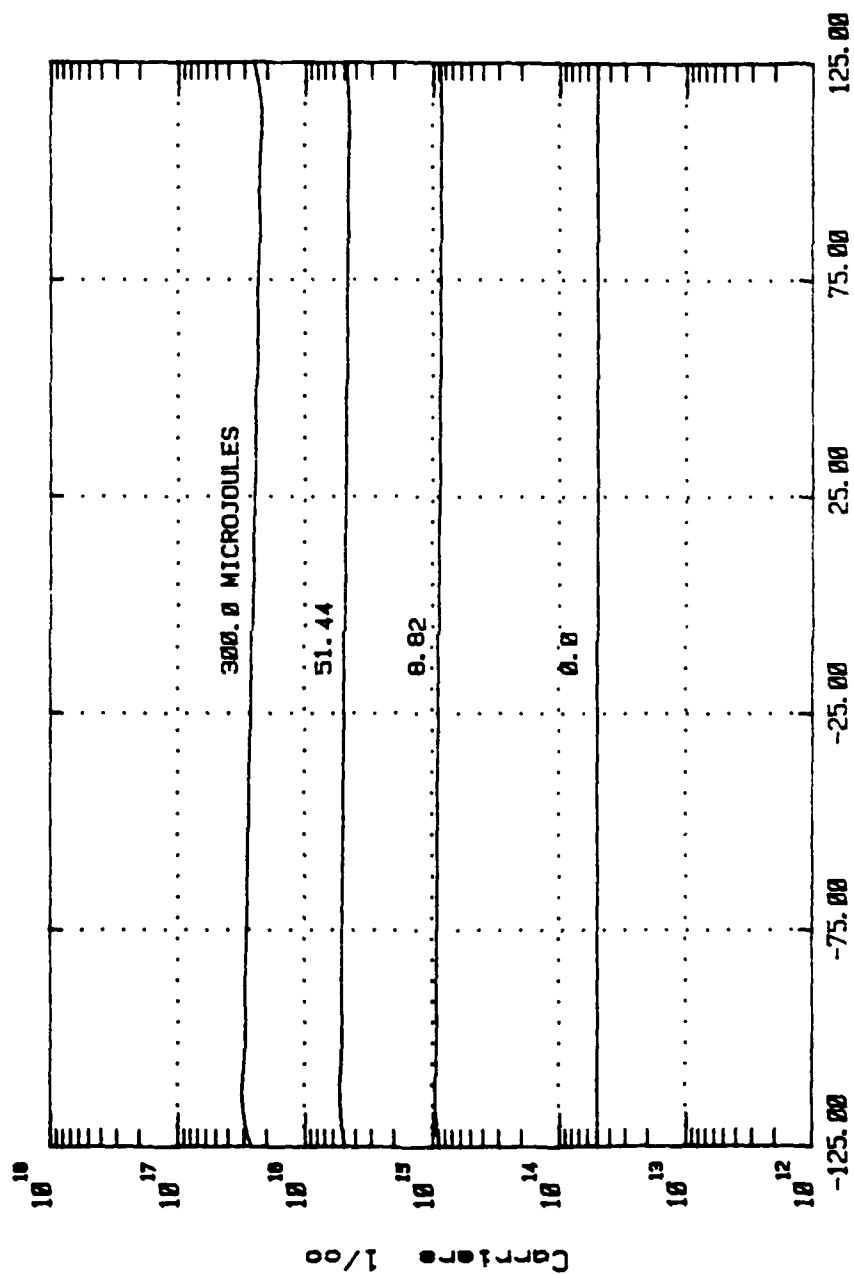
Figure 25    Calculated spatial distribution of electron-hole pair generation for three 1.06 µm light energies.

Sample thickness microns

T= 0.0 US

8.0

18.0

24.0

32.0

125.00

75.00

25.00

-25.00

-75.00

-125.00

$10^{18}$
$10^{17}$
$10^{16}$
$10^{15}$
$10^{14}$
$10^{13}$
$10^{12}$

Electron-hole Pairs 1/cc
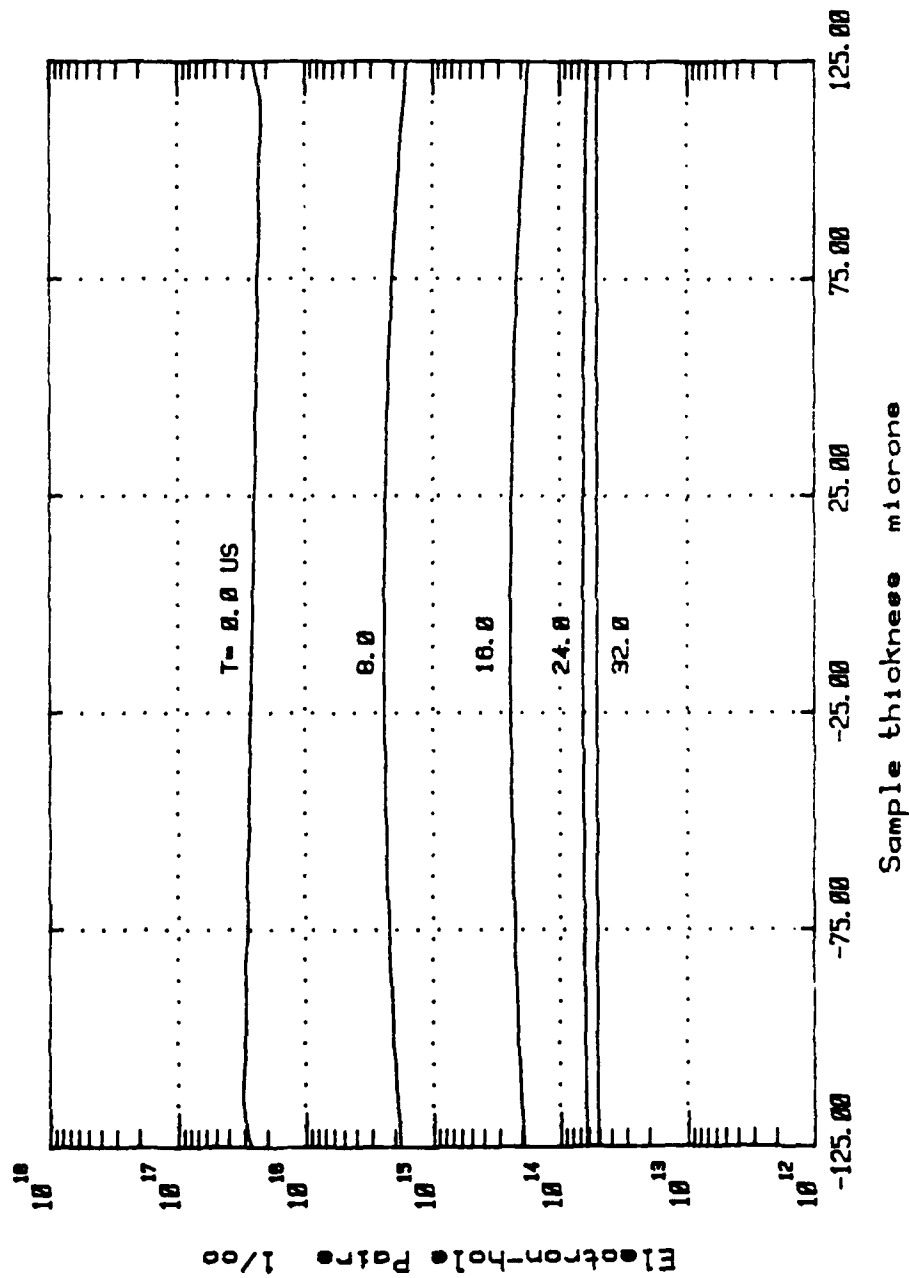
Figure 26    Calculated spatial distribution and time decay of electron-hole pairs for a 300 microjoule 1.06 ηm light pulse. Lifetime is 4.0 microseconds.
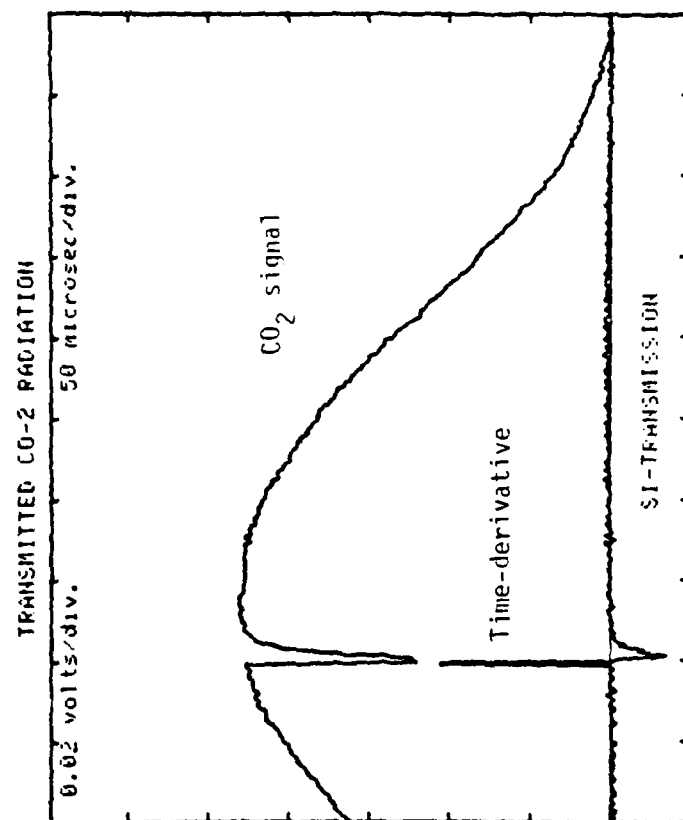
Figure 27    Experimental time-dependent modulation of transmitted $CO_2$ laser light.

67
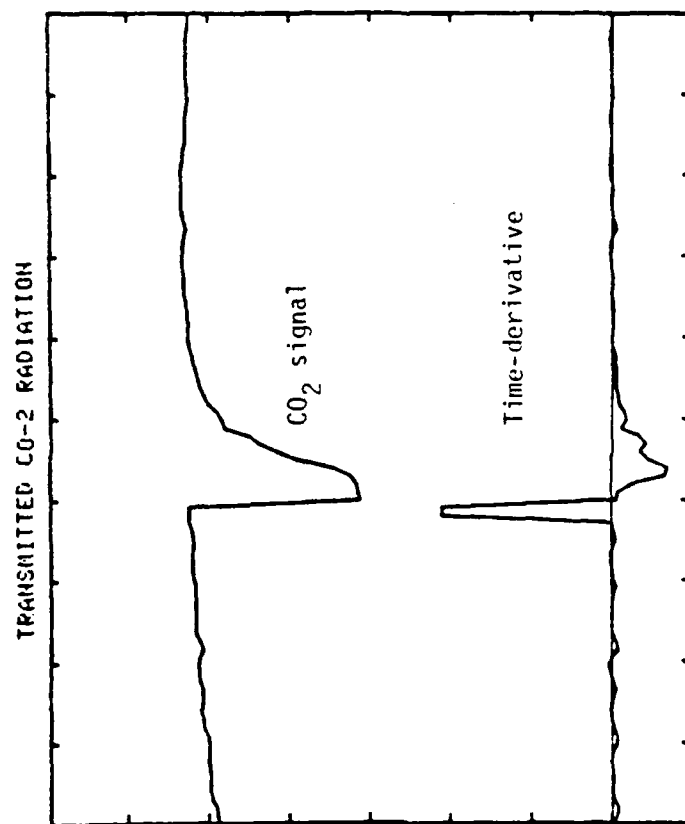
Figure 28  Computed time-derivative of expanded modulated $CO_2$ laser light. Time scale is 5.0 microseconds per division.

68

CO-2 LASER TRANSMISSION IN SILICON

5 microsec./div.

0.02 volts/div.

$\tau al = 4.0$ µsec

0.61mJ/cm$^2$

1.89mJ/cm$^2$

6.74mJ/cm$^2$

Ground level
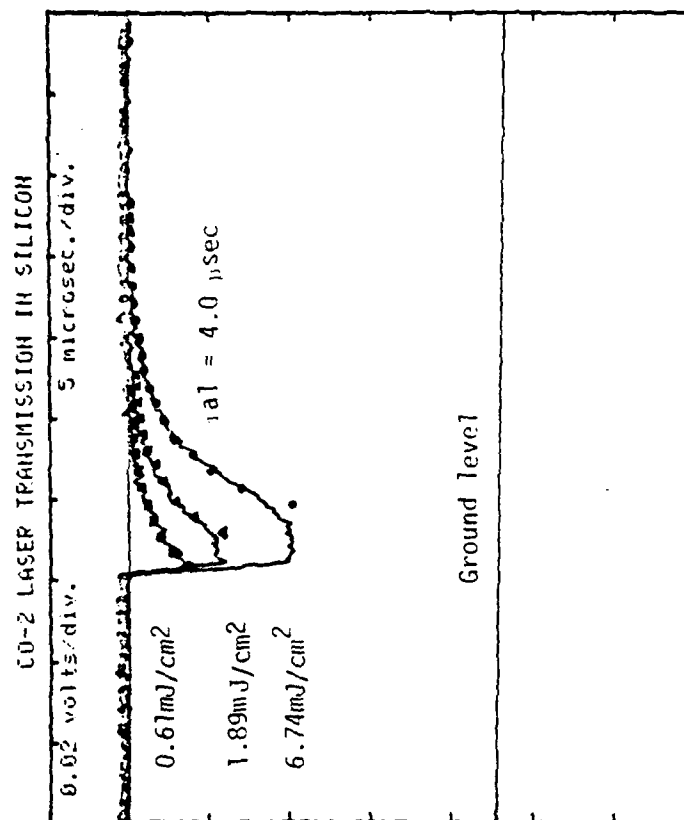
Figure 29    Experimental time-expansion of modulated $CO_2$ laser light for three levels of pump energies.  Calculated time-dependent solution is superimposed where a lifetime of 4.0 microseconds and a hole cross section of $8.14 \times 10-16$ CM-2 fits the experimental waveform.

TABLE 3.2 CONSTANTS

| 1.06 $\mu$m Radiation Constants | | |
|---|---|---|
| $\omega$ | $1.774 \times 10^{15}$ | $(sec)^{-1}$ |
| $\varepsilon_1, \varepsilon_2$ | $8.854 \times 10^{-14}$ | Farads/cm |
| $\mu_1, \mu_2, \mu_3$ | $4\pi \times 10^{-9}$ | Henries/cm |
| $\varepsilon_2^{\,'}$ | $1.036 \times 10^{-12}$ | Farads/cm |
| $d$ | $250.0 \times 10^{-4}$ | cm. |
| $\omega h$ | $1.871 \times 10^{-19}$ (1.172eV) | joules |
| $\beta_2$ | $2.03 \times 10^{5}$ | $(cm)^{-1}$ |
| $n$ | 3.5549 [27] | |
| $\lambda_s$ | 0.2982 $(\lambda_s = \frac{\lambda}{n})$ | $\mu$m |

dioxide should be able to maximize the transmission of the 1.06 μm energy at the first boundary [9,13]. Next, the absolute value of the square of the electric fields of the 1.06 μm radiation within the semiconductor can be found by using equations (1.22) and (1.23). As a result, the spatial distributions of the optically generated carrier density can be computed with equation (1.26). Figure 25 plots the carrier density as a function of distance and in-cident energies for time equal zero. Table 3.2 lists the constants utilized for the 1.06 μm radiation equations.

Immediately after the light pulse passes through the silicon wafer, the generated carriers will decay with an effective lifetime $\tau_a$. Equation (1.41) describes this redistribution of optically excited carriers and is graphed in Figure 26. The lifetime of the carriers can easily be matched to fit the temporal variation of the $CO_2$ signal beam. As a result, material lifetimes can easily be measured in this contact-less method.

The experimentally-observed modulated time-dependent $CO_2$ laser beam is shown in figure 27. A modulation near 50% is observable with a control laser energy of 300 microjoules. Superimposed on the same figure is the time-derivative of the $CO_2$ laser beam waveform. Clearly, the first derivative represents the occurence of the Nd:YAG laser pulse, while the second one of opposite polarity shows the lifetime associated with the decay of carriers. Figure 28 is a time expansion of Figure 27. It is clear that the risetime of the modulated infrared light is limited by the pyroelectric detector's response time. In addition, several different slopes are observed in the $CO_2$ laser waveform. These correspond to the multi-lifetime decay present in indirect band-gap materials such as silicon. Figure 29 is a time expansion of Figure 27

71

TABLE 3.3

| | 10.59 μm RADIATION CONSTANTS | |
|---|---|---|
| $\omega$ | $1.780 \times 10^{14}$ | $sec^{-1}$ |
| $h\omega$ | $1.877 \times 10^{-20}$ (0.1173) | joules |
| $\alpha$ | $1 - 10$ | $cm^{-1}$ |
| $\beta$ | $2.03 \times 10^{4}$ | $cm^{-1}$ |
| $d$ | $260 \times 10^{-4}$ | cm |
| $\sigma_f$ | $4.6 \times 10^{-17}$ (equation 1.49) | $cm^2$ |
| $\sigma_d$ | $8.14 \times 10^{-15}$ (experimental) | $cm^2$ |
| $\tau$ | 4.0 (experimental) | $\mu sec$ |

where the three waveforms correspond to three different incident energies from the control laser. A saturation effect is noticed as the pump energy is increased. This behavior can be attributed to the fact that only a fraction of the optically generated holes contribute to the absorption of the 10.59 μm radiation. There is narrow region in $\vec{k}$ space away from $\vec{k} = 0$ where direct transitions are allowed. If we move away from this region and opposite to $\vec{k} = 0$, the Maxwellian distribution function for the holes will become small, minimizing the probability of transitions [33,34]. As a result, as the electron-hole pairs recombine, a good number of holes are still available on top of the valence band for 10.59 μm absorption. These available holes are continuously shuffled around the top of the band by thermal scattering processes at picosecond rates. Table 3.3 lists constants pertaining to the calculation of the absorption of 0.59μm light.

Finally, Figure 29 also shows the theoretical results super-imposed over the experimental ones after readjusting for the saturation effect. Equations (1.41) and (1.48) are used where a lifetime of 4.0 microseconds was selected to fit all three waveforms. In addition, a hole cross section of $8.14 \times 10^{-16}$ centimeters squared resulted from the ex-perimental curves. This value is of the same order of magnitude as the ones published in the literature ($1.3-7.0 \times 10^{-16}$ cm$^2$) [31,32].

From obtained experimental results, one can conclude that modula-tion of 10 μm light may be accomplished with low levels of optically excited holes. This is due to their rather large cross section for materials such as silicon and germanium. One should point out that only a portion of these holes contribute to the absorption of 10 μm light. As

73

a consequence, the modulation depth is not only a function of hole density but it also depends on the number of 10 μm photons. That is, for larger signal beam power levels, larger control beam powers are required to obtain similar modulation depths.

## 3.4    SWITCHING IMPROVEMENTS

An optical switch based on silicon has one serious drawback: its switching speed. Due to the indirect nature of carrier decay via recombination centers, the lifetime of a free electron or hole is in the order of tens of microseconds. It is well known that this lifetime is inversely proportional to the level of recombination centers in an indirect band gap material such as silicon [38,39,40]. This relation may be written for

$$\gamma_n = \frac{1}{\sigma_n v_{thn} N_1} \tag{3.1}$$

where $N_1$ is the concentration of the centers per unit volume, $\sigma_n$ is their capture cross section for electrons, and $v_{thn}$ is the electron thermal velocity. Similarly, the expression for the hole lifetime is, inversely proportional to the level of recombination centers in an

$$\tau_p = \frac{1}{\sigma_p v_{thp} N_2} \tag{3.2}$$

Note that $N_1$ and $N_2$ are the densities of the two trapping levels associated with each gold atom [39]. $N_1$ is associated with an acceptor level located about 0.35 eV above the valence band and $N_2$ is the donor level located about 0.54 eV below the conduction band. This clearly suggests

74
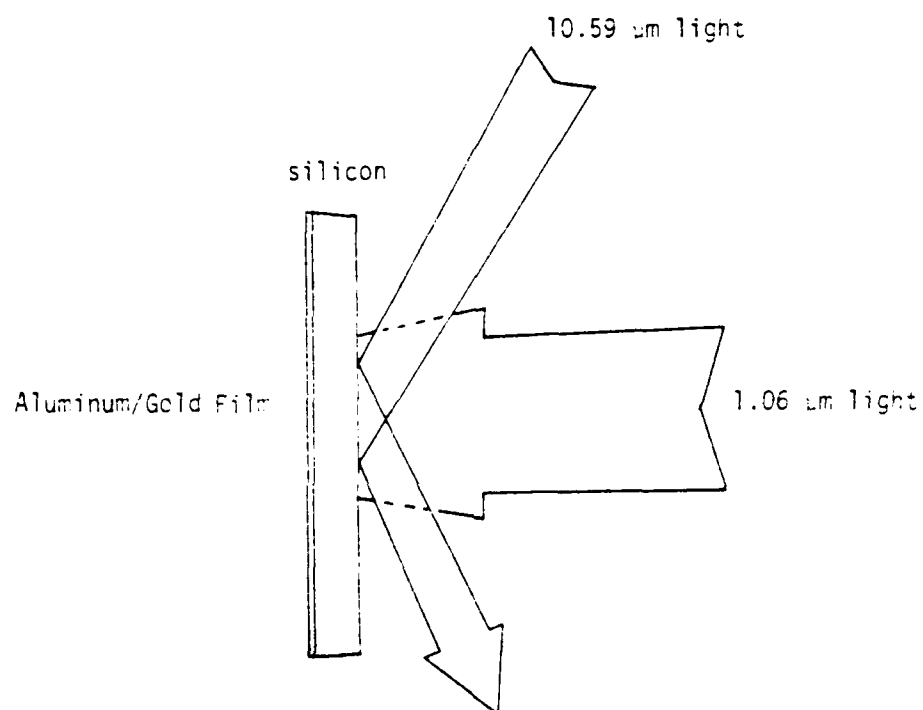
Figure 30    Experimental configuration for a gold-doped sample with a metallized back. Sample is at the Brewster angle with respect to the 10.59 um light.

CO-2 LASER TRANSMISSION IN SILICON

0.02 volts/div.          0.5 microsec./div.

$\tau a1 = 0.55$ µsec

Figure 31    Experimental time-dependent modulation of transmitted
$CO_2$ laser light in gold-oped sample. Calculated solution
is superimposed where a lifetime of 0.55 microseconds and
a hole cross section of $8.14 \times 10^{-16}$ $cm^2$ fits the experi-
mental waveform.

that to improve on the time response of an optical modulator based on p-type silicon, gold atoms should be introduced into the crystal lattice.

Gold is introduced into silicon in a controlled fashion by solid-state diffusion. A thin film of high purity gold ($\approx 200A$) is evaporated on a silicon sample from the same batch of wafers used for part C. The silicon wafer is inserted in a Lindberg diffusion furnace set at 900C. ($\approx 3 \times 10^{15}$ ATOMS/cc) [41]. In addition, a thin film of aluminum and gold is evaporated on one side of the polished silicon wafer.
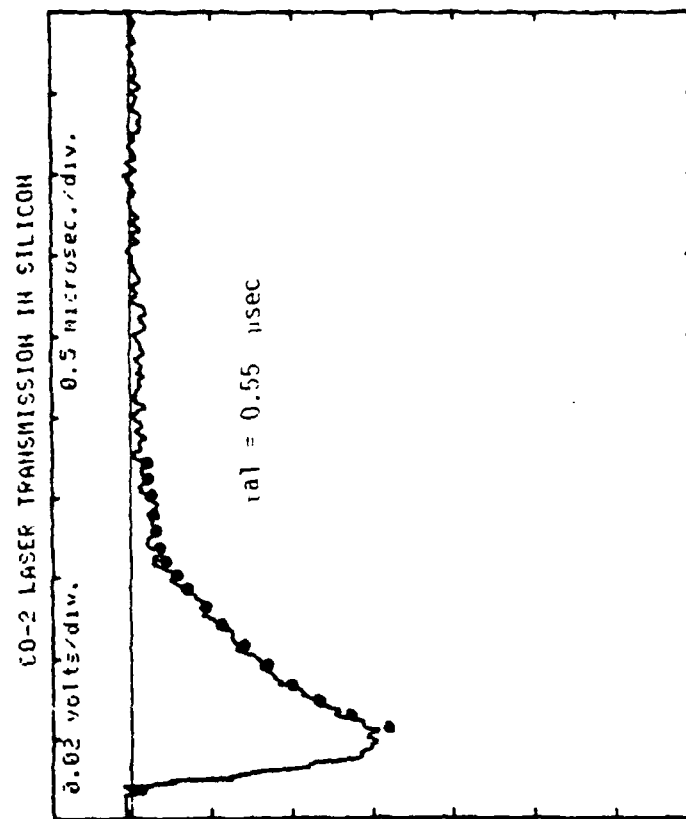
The metal backing on the sample provides a two-fold improvement over the previous experimental set-up. The optical path of both probing and controlling beams are increased. As a result, an improvement in the attenuation of the $CO_2$ laser probing beam is expected. Figure 30 illustrates the positioning of both laser beams with respect to the sample in which the signal's incidence orientation is maintained at the Brewster angle. Figure 31 shows the time-dependent waveform subjected to 300 microjoules of incident energy from the Nd:YAG control laser. Also superimposed on Figure 31 is the resulting theoretical waveform where a lifetime of 0.55 microseconds provides the best fit. Thus, an improvement of near one order of magnitude over the previous lifetime (4.0 microseconds) is obtained by introducing gold atoms into the silicon lattice.

The number of gold recombination centers can be increased by lengthening the diffusion time and increasing its temperature. As a consequence, much faster switching times may result (near 1 nanosecond).
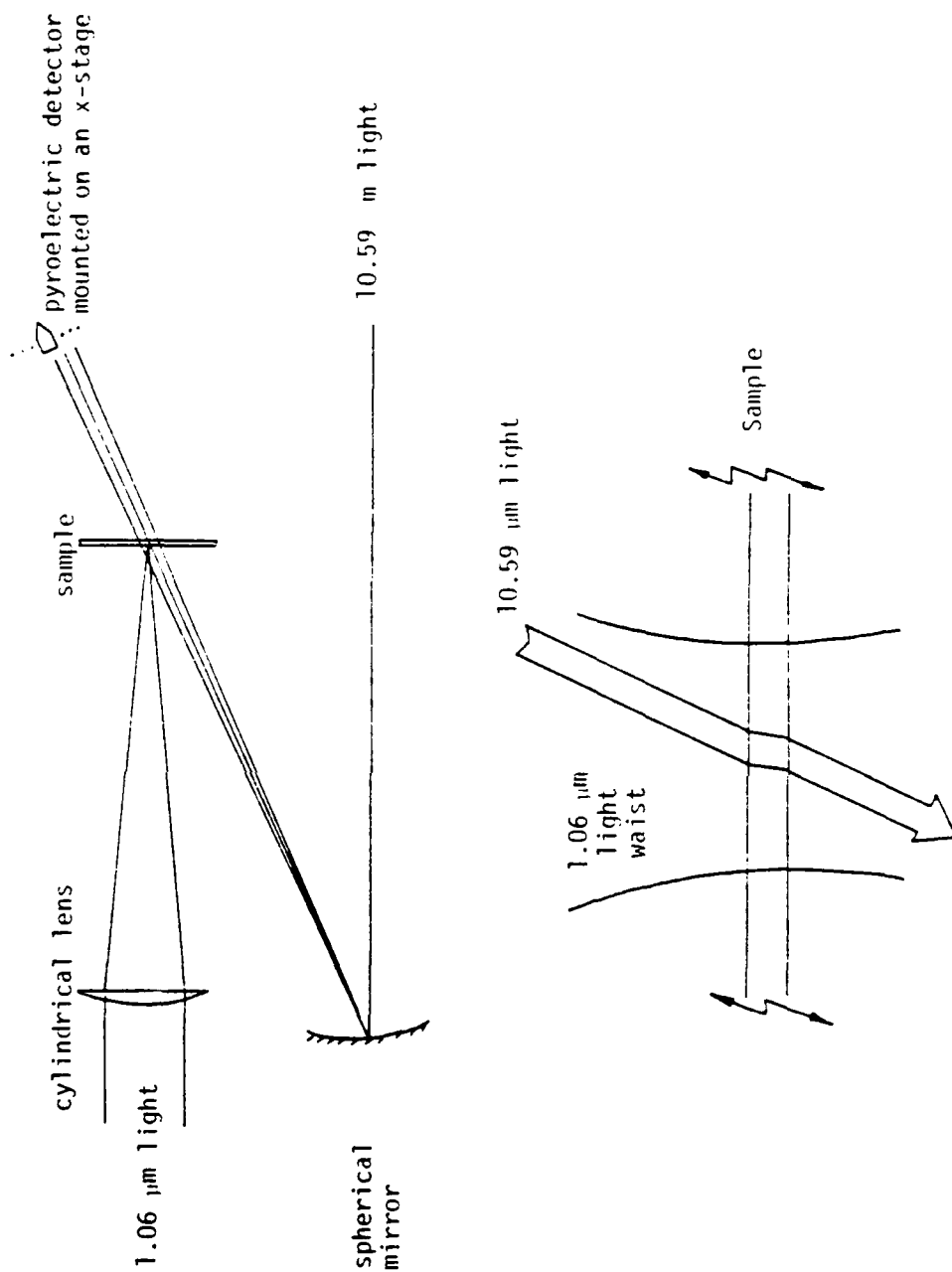
77

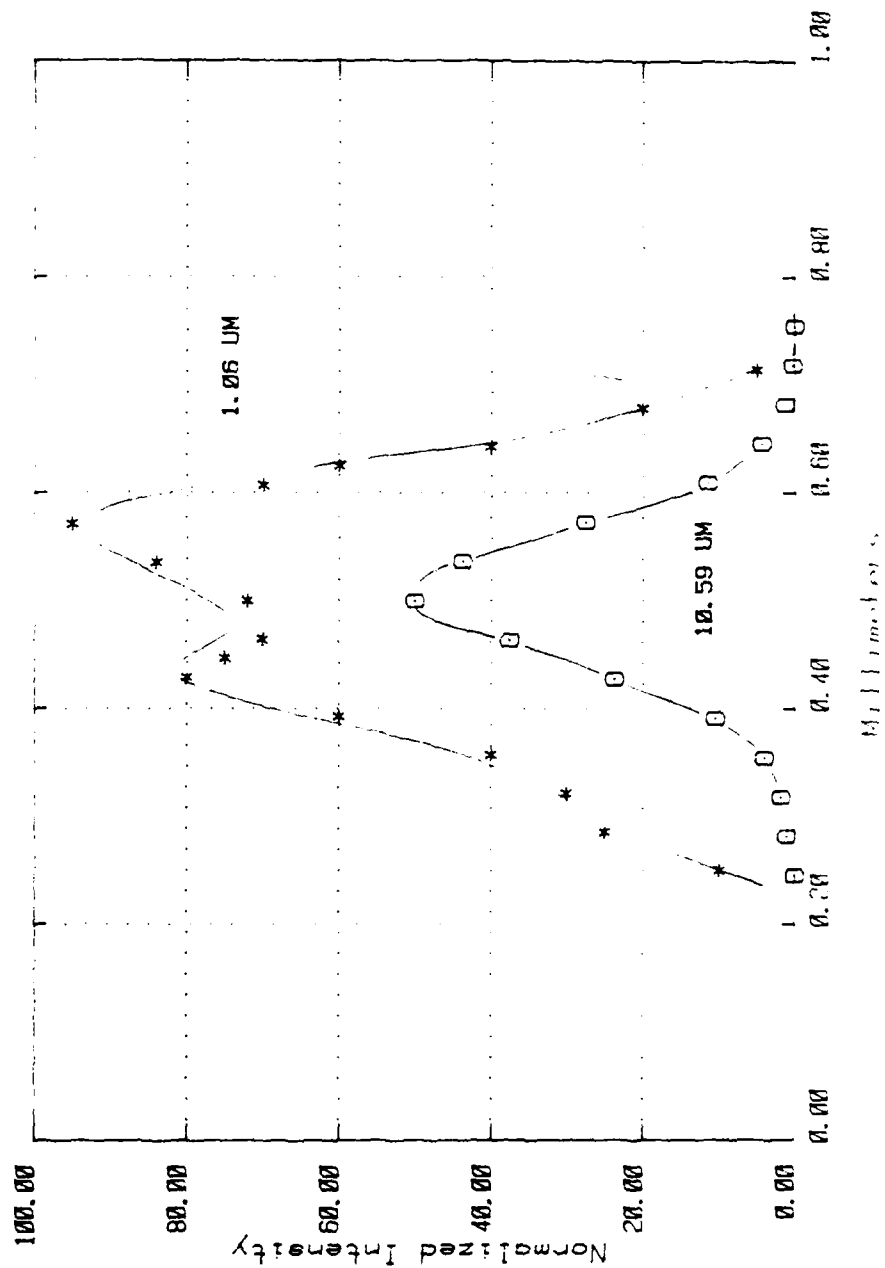Figure 32    Simple experimental layout to measure modulator resolution.

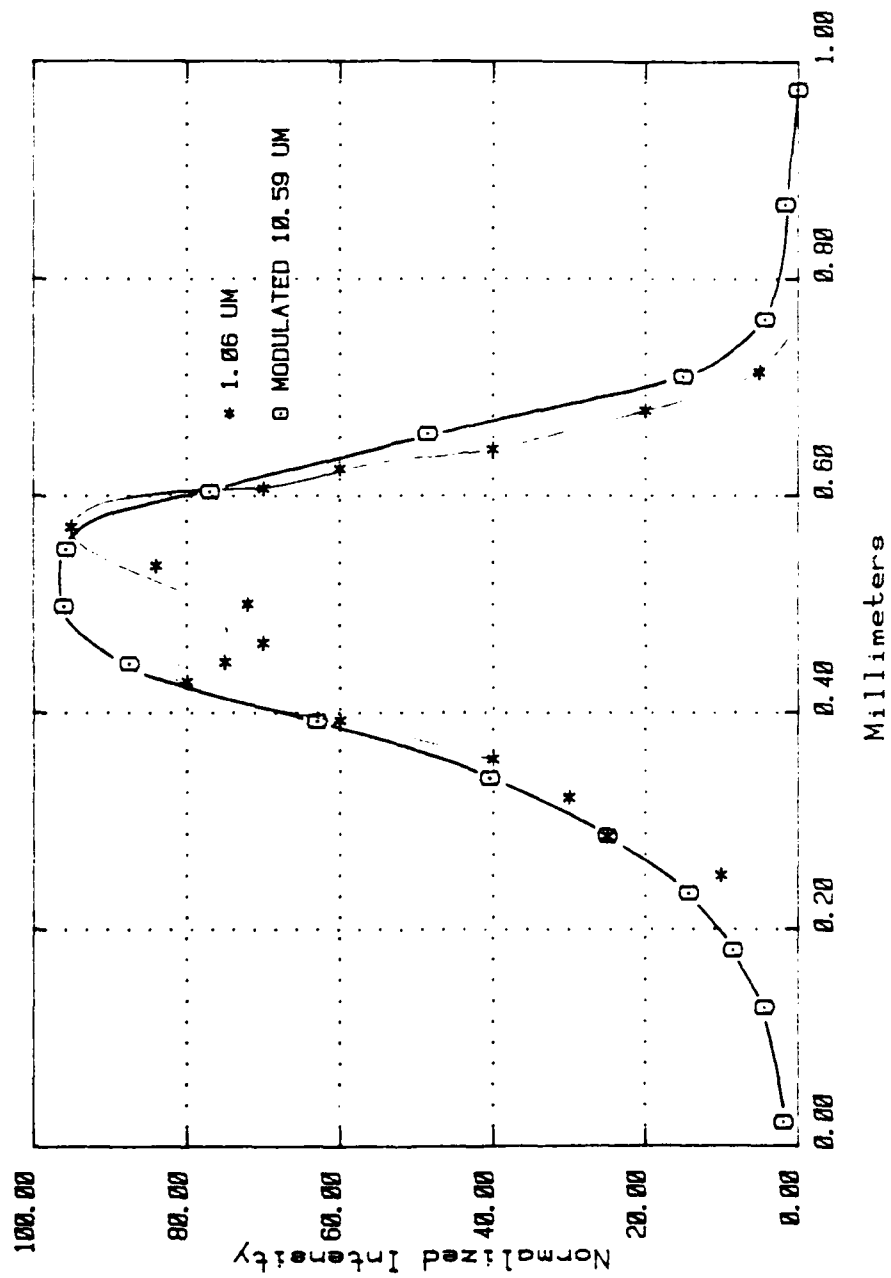Figure 33    Spatial distribution of both 10.59 μm and 1.06 μm radiation at the sample surface.

Figure 34    Modulation depth as a function of distance superimposed over 1.06 μm spatial
distribution.

## 3.5    RESOLUTION ESTIMATE

A complex experimental set-up consisting of array detectors for both wavelengths and imaging of a standard resolution pattern on the sample's surface is bypassed in favor of a simpler experimental lay-out as shown in Figure 32.    The basic premise is that this will provide preliminary resolution data without the need for an involved experiment.

The basic idea as portrayed in Figure 32 is to focus the control laser's beam with a cylindrical lens on the sample's surface depicting a narrow line.    Then by scanning a well focused probing beam in and out of the carrier generation region a plot of the percent modulation as a function of space is produced.    Clearly, the $CO_2$ laser's spot size must be equal or less than the Nd:YAG laser's focused line.    As a result, the expected spatial modulation follows the control laser's spatial intensity.

The spatial distributions for both probing and controlling beams are shown in Figure 33.    These are obtained by scanning a pyroelectric and a PIN diode across expanded 10.59 μm and 1.06 μm beams respectively.    The actual spatial dimensions result from burnt patterns made on polaroid film.    It should be pointed out that this method is not reliable in measuring laser spot sizes and it is only used to insure that the 10.59 μm spot size is less than the 1.06 μm light at the sample's position.    The normalized modulation of the $CO_2$ laser probing beam and the spatial distribution of the Nd:YAG  control beam is plotted in Figure 34 as a function of distance.    Clearly, the modulated 10.59 μm light follows the shape of the 1.06 μm light indicating a direct transfer of spatial information from one light source to another.    Unfortunately, the spatial resolution is only about 2 lines per millimeter.    This, of course, is limited by the control laser's optics and not the sample's characteristics.

## 4.  CONCLUSIONS

Several conclusions may be drawn from the hole pumping experiments. To begin with, the feasibility of modulation of one light source by another via the optical generation of carriers in a semiconductor has been demonstrated. This result provides the basis for a spatial light modulator for the 10 µm wavelength region. Close to 50% modulation was achieved with relatively low energy density (6.73 mJcm$^{-2}$) originating from the control laser. This suggests that other light sources of reasonable power output could be used as control sources provided their photon energies were slightly larger than the semiconductors' band-gap energy.

A saturation effect was noticed in the time-dependent signal waveform. This phenomenon is due to the selective participation of free holes in the absorption of 10.59 µm radiation. That is, only the portion of the free holes near the top of the valence band which are located in the vicinity of the 10.59 µm light energy contribute to direct intra-valence band transitions. As a result, the attenuation of the $CO_2$ laser beam was sustained until the non-participating holes on top the valence band were filled with the decaying free electrons.

A theoretical fit to experimental data provided an effective lifetime of 4.0 microseconds for the high-resistivity material used. By the introduction of additional recombination centers into the lattice, the carrier lifetime was reduced to 0.55 microseconds. This in turn, improved the switching time of the light modulator from 15 microseconds down to near 1 microsecond for a modulation depth of 50%. Additional gold centers should further decrease the switching time into the nano-second region. As a result, wideband optical modulation may be attained with gold-doped silicon.

According to the simple resolution experiments, a resolution of 2 lines per millimeter can be obtained using the 4.0 microsecond material. Because of the inability to provide a well focused control beam to the sample, this resolution figure does not represent the sample's maximum resolving power. Further experiments are necessary.

An inherent feature of a silicon-based optical light modulator is its simple structure. An antireflection coating for the control beam could improve device performance by reducing control beam energy requirements. A thermally grown silicon-dioxide film could be used for the Nd:YAG laser [28]. Simple fabrication requirements are an attractive feature for spatial light modulator implementation.

Several topics that merit further investigation have become apparent during the experimental phase of this work. Lifetime studies in silicon are possible with this contactless method. Previous experimental configurations have relied on fabrication of p-n junctions to observe the decay of the generated carriers. More recently, contactless methods have been used in which a 10 Gigahertz microwave is utilized as a probing signal [35,36]. Because all the semiconductor samples need to be mounted within a waveguide, these schemes tend to be cumbersome. It is believed that the configuration used in this work provides ease of implementation for lifetime studies.

In addition to contact-less lifetime studies, work should be directed into identifying and separately measuring the several absorption mechanisms occuring in silicon near 10 microns. Futhermore, competing mechanisms associated with the optical generation of electron-hole pairs and their decay via recombination centers could be studied. Finally,
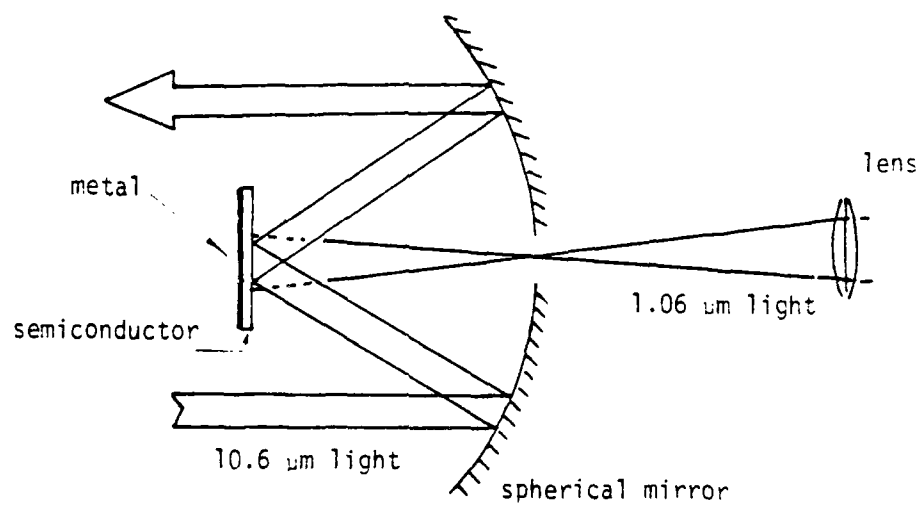
83

Figure 35    Optical switch configuration based on a
             semiconductor crystal. 10 um light con-
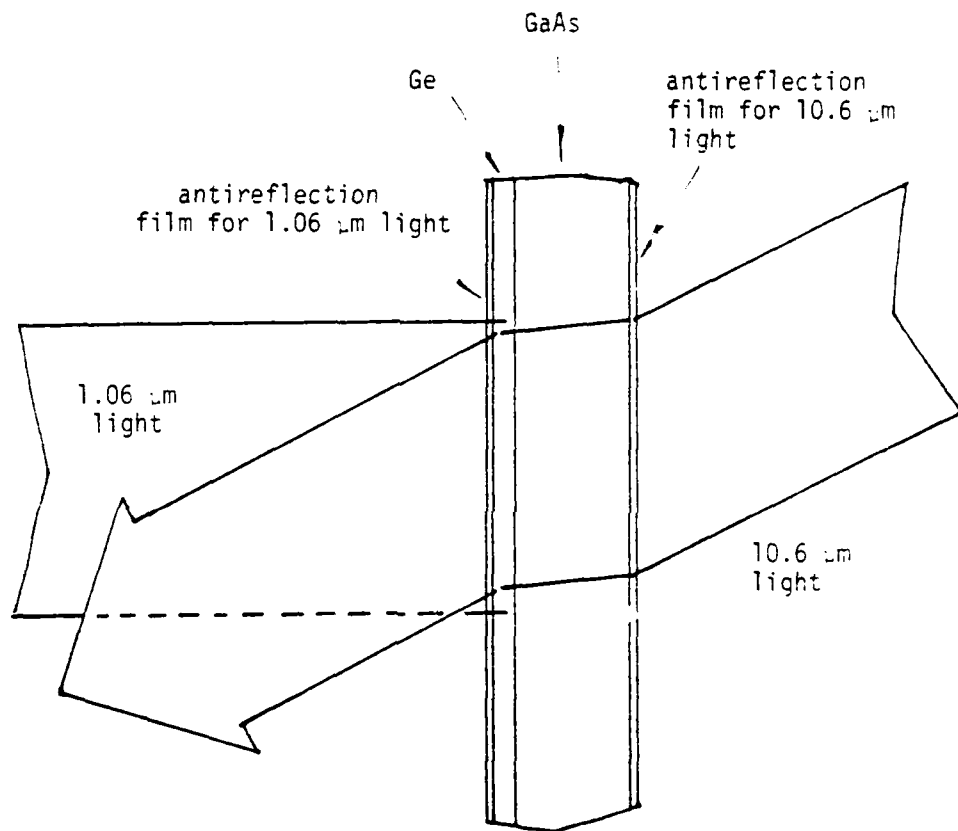             trolled by 1.06 um light.

84

Figure 36    Optical spatial light modulator operating near 10 μm
             light.  Germanium film deposited on a GaAs substrate.

valence band structure could be verified with a tunable $CO_2$ laser as the probing signal. The basic premise in these suggestions is that semi-conductor processes can be studied in a non-destructive manner with electromagnetic radiation.

A more detailed resolution study on such an infrared SLM is required to provide additional feasability information. Specifically, a standard resolution pattern should be imaged on the surface of the crystal with the help of a lens. In addition, the control laser's beam should be collimated and spatially filtered to obtain a clean wavefront. Furthermore, the $CO_2$ laser's probing beam should also be collimated and filtered. Finally, array detectors must be employed to get an accurate spatial signal from such an infrared SLM.

Several applications are possible with a semiconductor-based optical switch. The simplest one would consist of a one-dimensional optical modulator in which a high-powered CW $CO_2$ laser is controlled by a pulsed Nd:YAG laser. Large bandwidths are possible if proper lifetime-reduction techniques are employed in silicon. Figure 35 snows a probable arrangement where multiple passes of the controlling beam may reduce its energy density requirement.

A more complex implementation of a spatial light modulator is depicted in Figure 36. In this particular instance, a 10 to 20 μm film of germanium (Ge) grown or deposited on a gallium arsenide (GaAs) sub-strate could provide larger modulation depths. This results from the fairly large absorption coefficient of Ge at 1.06 μm. Optical switching is still based in the optical generation of free carriers which would absorb radiation near 10 μm by direct intravalence band transitions. The GaAs crystal is utilized only as a substrate due to its transparency at

both wavelengths of interest.  In addition, Ge can easily be grown over
such a substrate.

## CARRIER REDISTRIBUTION (one dimension)

The second order differential equation that describes the decay of electron-hole pairs may be stated in its ambipolar form as,

$$\frac{\delta n'}{\delta t} = -\frac{n'}{\tau_a} + D_a \frac{\delta^2 n'}{\delta z^2} \tag{A.1}$$

where n' represents the number of electron-hole pairs per cubic centimeter and $\tau_a$ and $D_a$ represent their ambipolar lifetime in seconds and their diffusivity in centimeter squared per second respectively.

If the number of carriers is expressed as the product of two independent functions,

$$n'(z,t) = Z(z) T(t) \tag{A.2}$$

we obtain,

$$\frac{1}{T} \frac{\delta T}{\delta t} = -\frac{1}{\tau_a} + D_a \frac{1}{Z} \frac{\delta^2 Z}{\delta z^2} \tag{A.3}$$

by direct substitution of equation (A.2) into (A.1). As a result, we may write,

$$\frac{1}{Z} \frac{\delta^2}{\delta z^2} = -C^2 \tag{A.4}$$

and

$$\frac{1}{T} \frac{\delta T}{\delta t} = -\nu \tag{A.5}$$

END
DATE
FILMED

DTIC
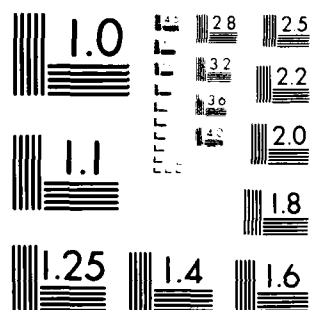
MICROCOPY RESOLUTION TEST CHART

NATIONAL BUREAU OF STANDARDS 1963 A

whose individual solutions lead to the overall expression for $n'(z,t)$,

$$n'(z,t) = (A \cos(cz) + B \sin(cz))\varepsilon^{-\nu t} \qquad (A.6)$$

where

$$\nu = \frac{1}{\tau_a} + D_a c^2 \qquad (A.7)$$

A linear superposition of solutions of the form of equation (A.6) such as,

$$n'(z,t) = \sum_{k=0}^{\infty} (A_k \cos(C_k z) + B_k \sin(C_k z))\varepsilon^{-\nu_k t} \qquad (A.8)$$

and

$$\nu_k = \frac{1}{\tau_a} + D_a C_k^2 \qquad (A.9)$$

will satisfy the differential equation where the values of $A_k$, $B_k$, and $C_k$ may be chosen so that the boundary conditions are satisfied by the super-position.

The surface boundary conditions are,

$$\mp D_a \frac{\delta n'}{\delta z} \bigg|_{z = \pm d} = s n'(\pm d, t) \qquad (A.10)$$

where s is the surface recombination velocity in centimeters per second and 2d is the thickness of the semiconductor slab. Substituting a solution of the form of equation (A.6) into (A.10) we find that in order to satisfy equation (A.10) we need to solve the transcendental equation,

$$ctn(C_k d) = \frac{D_a}{ds} (C_k d). \qquad (A.11)$$

89

Note that for a very good surface (s = 0), $C_k d = k\pi$ where $k = 0,1,2,3$, and for a lapped surface (s = ∞) $C_k d = (2k + 1) \pi/2$ where $k = 0,1,2,3...$

The third boundary condition provides us with the carrier distribution as a function of z for time equal zero, (refer to equation (1.26)).

$$n'(z,0) = n^+ \varepsilon^{-2\alpha_2(z+d)} + n^- \varepsilon^{2\alpha_2(z+d)} \tag{A.12}$$

where,

$$n^\pm = \frac{\beta 2\alpha_2}{\omega^2 \mu n} \left| \varepsilon_2^\pm \right|^2 . \tag{A.13}$$

By setting equation (A.9) equal to (A.12) we may determine the coefficients $A_k$ and $B_k$. We write,

$$\sum_{k=0}^{\infty} \left( A_k \cos(C_k z) + B_k \sin(C_k z) \right) = n'(z,0) \tag{A.14}$$

By multiplying both sides of equation (A.14) by $\cos(C_\ell z)$, integrating over the entire thickness of the slab, and using the orthogonality principal,

$$\int_{-d/2}^{d/2} \cos(C_k z) \cos(C_\ell z) dz = 0 \tag{A.15}$$

for $k \neq \ell$, we obtain an expression for $A_k$,

90

$$A_k = \frac{2C_k}{4\alpha_2^2 + C_k^2} \quad \frac{1}{2C_k d + \sin(2C_k d)}$$

$$\times \left[ C_k \sin(C_k d) \left\{ n^+ (1 + \epsilon^{-4\alpha_2 d}) + n^- (1 + \epsilon^{4\alpha_2 d}) \right\} \right.$$

$$\left. + 2\alpha_2 \cos(C_k d) \left\{ n^+ (1 - \epsilon^{-4\alpha_2 d}) - n^- (1 - \epsilon^{4\alpha_2 d}) \right\} \right] \quad . \qquad (A.16)$$

Similarly, to obtain $B_k$, we multiply both sides of (A.14) by $\sin(k_\ell z)$, integrate, and use the orthogonality principal. As a result, we have,

$$B_k = \frac{1}{d} \frac{1}{4\alpha_2^2 + C_k^2}$$

$$\times \left[ C_k \cos(C_k d) \left\{ n^+ (1 - \epsilon^{-4\alpha_2 d}) + n^- (1 - \epsilon^{4\alpha_2 d}) \right\} \right.$$

$$\left. - 2\alpha_2 \sin(C_k d) \left\{ n^+ (1 + \epsilon^{-4\alpha_2 d}) - n^- (1 + \epsilon^{4\alpha_2 d}) \right\} \right] \qquad (A.17)$$

APPENDIX B

MOBILITY DEPENDENCE ON CARRIER LEVEL

The mobility of an electron or hole within a semiconductor is a function of three components: the lattice mobility, the impurity scattering mobility, and the hole-electron scattering mobility [26]. The coulomb interaction of the impurity scattering component and the hole-electron scattering component are combined in a reciprocal law to give a mobility $\mu_c$,

$$\frac{1}{\mu_c} = \frac{1}{\mu_I} + \frac{1}{\mu_{he}} \tag{B.1}$$

where $\mu_I$ and $\mu_{he}$ are the impurity and hole-electron scattering mobilities.

The effective mobility is obtained by combining $\mu_c$ and the lattice mobility $\mu_L$ using a reciprocal law,

$$\frac{1}{\mu} = \frac{1}{F} \frac{1}{\mu_c} + \frac{1}{\mu_L} \tag{B.2}$$

where the statistical factor F is defined as,

$$F = \frac{0.0954 + 0.473Z - 0.383z^2}{0.0956 + 0.866z - 0.776z^2} \tag{B.3}$$

and,

$$z = \frac{\mu_L}{\mu_L + \mu_C} .$$
(B.4)

The expressions for $\mu_I$, $\mu_{he}$, and $\mu_L$ in $cm^2$/volt-sec are as follows:

$$\mu_I = \frac{2.45 \times 10^{21} \left(\frac{T_L}{300}\right)^{1.5}}{N \cdot \ell n \left[1 + \frac{1.41 \times 10^{20}}{n+p} \left(\frac{T_L}{300}\right)^2\right]}$$
(B.5)

$$\mu_{hen} = \frac{2.45 \times 10^{21} \left(\frac{T_L}{300}\right)^{1.5}}{\sqrt{2} \, p \, \ell n \left[1 + \frac{1.41 \times 10^{20}}{n+p} \left(\frac{T_L}{300}\right)^2\right]}$$
(B.6)

$$\mu_{hep} = \mu_{hen} \frac{p}{n}$$
(B.7)

$$\mu_{LP} = 480 \left(\frac{T_L}{300}\right)^{-2.4}$$
(B.8)

$$\mu_{LP} = 480 \left(\frac{T_L}{300}\right)^{-2.5}$$
(B.9)

where N is the doping density, n and p are the free electron and hole density, $T_L$ is the lattice temperature in degrees Kelvin, and the small n and p subscripts refer to electron and hole mobilities respectively.

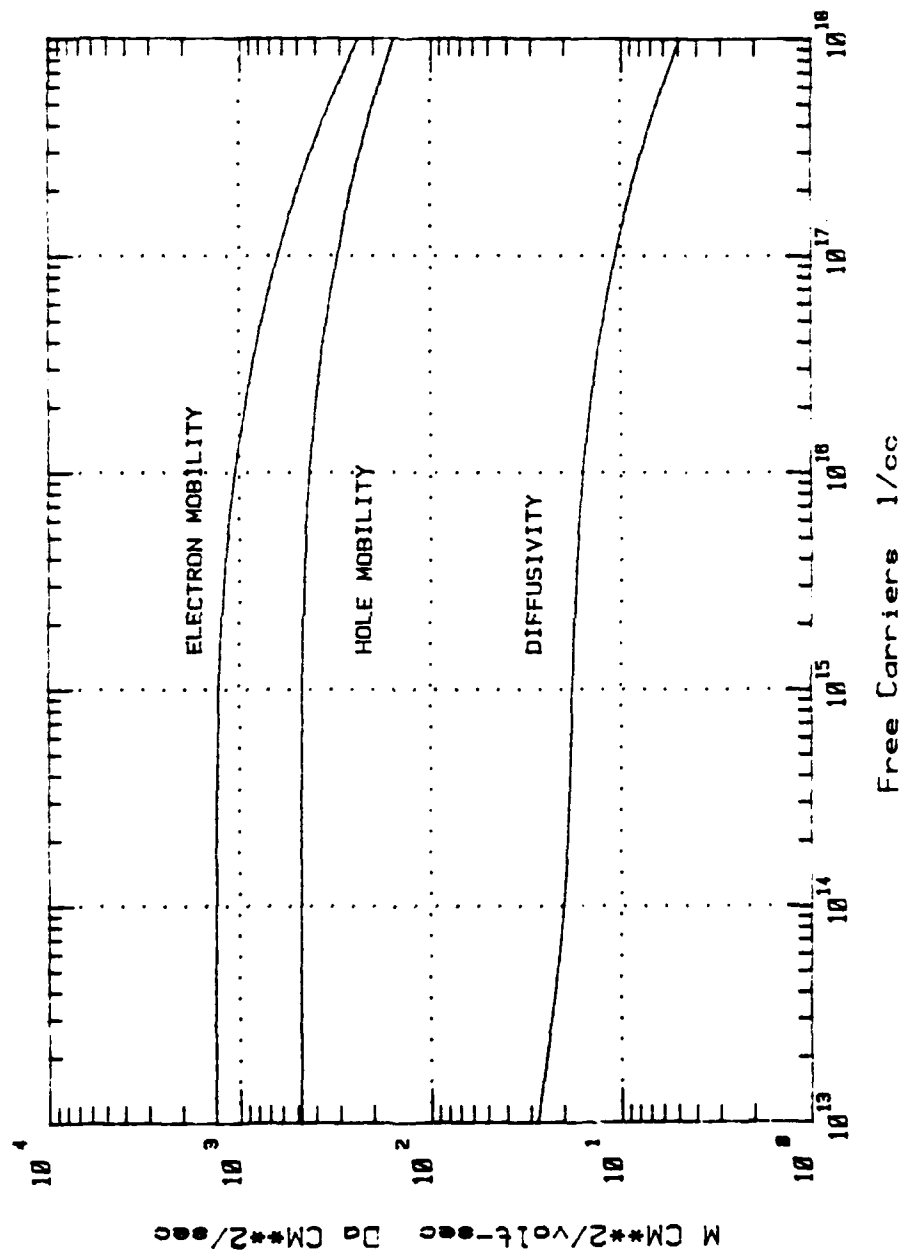Figure 37    Electron and hole mobilities and ambipolar diffusivity in silicon as a function of carrier density.

According to equation (1.39) the ambipolar diffusivity may be expressed as a function of the free carrier densities and their respective diffusivities,

$$Da = \frac{p + n}{\dfrac{n}{D_p} + \dfrac{p}{D_n}} \quad . \tag{B.10}$$

Figure 37 shows the ambipolar diffusivity as a function of free-carrier density level.

APPENDIX C

COMPUTER PROGRAM DESCRIPTION

Several computer programs are utilized in this work to obtain
several coefficients from experimental data.  In addition, to compare
theoretical and experimental results the solution of the superposition
that describes the decay of the optically generated carriers is imple-
mented in a program.  All the programs are written in Fortran and imple-
mented in a PDP 11V03-L minicomputer.  Double precision and complex
arithmetic are used where needed.  A brief description of each program is
included.  Listings may be obtained on request.

The absorption coefficients in silicon at a wavelenth of $1.06 \mu m$ are
determined from an experimental reflection and transmission coefficients
using equations (1.6) through (1.13).  The parameter $\epsilon_2^{''}$ is varied until
the computed value for $R_0$ and $T_0$ matches the experimental ones.   The
coefficients $|E_2^+|^2$ and $|E_2^-|^2$ can then be obtained using equations (1.22)
and (1.23). The aforementioned equations are implemented in programs
TVER.FOR and VER.FOR.

The time-dependent modulation of the $CO_2$ laser signal beam is
theoretically solved in several steps.  The electron-hole density is
first averaged as a function of distance.  This facilitates the calcula-
tion of the ambipolar diffusivity which is a function of carrier density
and the hole cross section at 10.59 μm.  Equations (1.41), (1.42), and
(1.48) are used.  Subroutine CKD1.FOR computes the coefficients $A_k$, $B_k$,
and $C_k$ used in equations (1.41) and (1.42); subroutines AVDIFF.FOR and
PARM.FOR compute the average level of carrier density and the ambipolar

96

diffusivity respectively. Note that the averaging of the carrier level is only done to obtain average values for the ambipolar diffusivity and the hole cross section. Program BIG.FOR finally calculates the attenuation of the $CO_2$ laser probe using an iterative method where a 1.0 μm increment is used. This scheme is used because of the nonuniform spatial distribution of the carrier density.

In all the theoretical calculations the value for the carrier lifetime and the surface recombination velocity are adjusted to fit the experimental results. A lifetime of 4.0 microseconds and a surface recombination velocity of 1000 cm/second results in the best fit.

The following two program listings are Basic programs originally developed by Mike Poirier at the ElectroScience Laboratory from The Ohio State University. They have been revised and updated by the author. These programs are used in conjunction with the Tektronix 4051 microcomputer and 7912 AD transient digitzer for data acquisition.

REFERENCES

1.  Christensen, C.R., private communication.

2.  Gara, Aaron D., "Real-time Optical Correlation of 3-D Scenes", Appl.
    Opt. 16, 149 (1967).

3.  Christensen, C.R., D.J. Upatnieks, and B.D. Guenther, "Vehicle
    Identification and Tracking Using a Coherent Optical Correlator",
    Technical Report T-79-18, US Army Missile Research and Development
    Command, DRDMI-TRO, Redstone Arsenal, Alabama, 35809.

4.  Collins, S.A., Jr., Proc. Photo-Opt. Instrum. Eng., 128 (1977).

5.  Franz, W., Naturforsch, 13A, 494 (1958).

6.  Keldysh, L.V., Zh. Eksp. Teor.Fiz. 34, 1138 (1958).

7.  Dyment and Kapron, Jour. Appl. Phys. 47, 1523-1528 (1976).

8.  Beneking, Grote and Svilans, IEEE Trans. on Elect. Dev., ED-28,
    404-407 (1981).

9.  Moss, Optical Properties of Semiconductors, Chapters 3, 5;
    Butterworths, 1959.

10. Ambroziak, Semiconductor Photoelectric Devices, Chapter 5, p. 77;
    I Liffe Books, 1968.

11. Grove, Physics and Technology of Semiconductor Devices, Chapter 5, p.
    124, John Wiley & Sons, 1967.

12. P.K. Tien, et.Al., Appl. Phy. Lett. 21, 8, p. 394 (1972).

13. A. Ashkin, J.M. Dziedzic, Appl. Phy. Lett. 21, p. 253 (1972).

14. Maiz, J.A., Optical Bistability in Bismuth Substituted Garnets, M.Sc.
    Thesis, The Ohio State University (1980).

15. Grischkowsky, D., et.al., Physical Review A, 12 (1975).

16. Maiz, J.A., Internal report, Electron Device Lab, OSU (1980).

17. B. de Cremoux, E. Leiba "Free Carrier Absorption for $10\mu$ Modulation", IEEE Proceedings, p. 1674-1675, Sept. 1969.

18. J. Benoit, "$CO_2$ Laser Modulation by Hole Injection in n-Type InSb", Applied Physics Letters, Vol. 16, pp. 482-484, June 1970.

19. D.H. Seib, H.M. Stoll, "Fast Optical Modulation of $10.6\mu m$ Radiation in GaAs Waveguides by Electrical Injection", IEEE Journal of Quantum Electronics, pp. 305-306, April 1977.

20. J.H. McFee, R.E. Nahory, M.A. Pollack, "Beam Deflection and Amplitude Modulation of $10.6\mu m$ Guided Waves by Free-Carrier Injection in GaAs-ALGaAs Meterostructures", Applied Physics Letters, Vol. 23, No. 10, pp. 571-573, Nov. 1973.

21. F. Keilmann, J. Kuhl, "Broadband Modulation of $3\ \mu m$ Light by $10\ \mu m$ Light in p-Germanium", IEEE Journal of Quantum Electronics, Vol. QE-14, No.3, pp. 203-206, Mar. 1978.

22. N. Kaiser, R.J. Collins, H.Y. Fan, "Absorption of Infrared Light by Free Carriers in Germanium", Physical Review, Vol. 91, p. 1342, 1953.

23. A.H. Kahn, "Theory of the Infrared Absorption of Carriers in Germanium and Silicon", Physical Review, Vol. 97, p. 1647, 1955.

24. J.A. Stratton, Electromagnetic Theory, McGraw-Hill Book Company, 1941.

25. S.K. Ghandhi, Semiconductor Power Devices, Wiley-Inter Science, 1977.

26. J.P. McKelvey, Solid State and Semiconductor Physics, Harper and Row, 1971.

27.  F. Berz, R.W. Cooper, S. Fagg, "Recombination in the End Regions of PIN Diodes", Solid State Electronics, Vol. 22, pp. 293-301, 1979.

28.  A. Ambroziak, <u>Semiconductor Photoelectric Devices</u>, London Iliffe Books Ltd., 1968.

29.  F.A. Johnson, "Lattice Absorption Bands in Silicon", Proceedings Physical Society, Vol. 73, pp. 265-272, 1958.

30.  R.B. James, D.L. Smith, "Saturation of Intervalence-band Transitions in p-type Semiconductors", Physical Review B, Vol. 21, No. 8, pp. 3502-3512, 1980.

31.  H. Hara, Y. Nishi, "Free Carrier Absorption in p-type Silicon", Journal Physical Society Japan, Vol. 21, p. 1222, 1966.

32.  R.B. James, D.L. Smith, "Absorption of High Intensity $CO_2$ Laser Light in p-type Semiconductors with Small Spin-Orbit Splittings", Journal Applied Physics, Vol. 52, No. 6, pp. 4238-4240, 1981.

33.  E.O. Kane, "Energy Band Structure in p-type Germanium and Silicon", Journal Physics and Chemistry of Solids, Vol. 1, pp. 82-89, 1956.

34.  F. Keilmann, "Infrared Saturation Spectroscopy in p-type Germanium", IEEE Journal of Quantum Electronics, Vol. QE-12, No. 10, pp. 592-597, 1976.

35.  C. Kittel, <u>Introduction to Solid State Physics</u>, John Wiley and Sons, 1966.

36.  R. White, J. Bernstein, "A Simple Contactless Microwave Method for measuring Carrier Lifetime During Solar-Cell Fabrication", IEEE Transactions on Electron Devices, Vol. ED-26, No. 11, 1979.

37.  H.K. Brown, "The Use of Microwaves to Characterize Optically Stimulated Semiconductors", Dissertation, The Ohio State University, 1980.

100

38. A.S. Grove, <u>Physics and Technology of Semiconductor Devices</u>, John Wiley and Sons, 1967.

39. A.E. Bakanowski, J.H. Forster, "Electrical Properties of Gold-Doped Diffused Silicon Computer Diodes", The Bell System Technical Journal, Vol. 39, No. 1, pp. 87-104, January 1960.

40. W. Shockley, W.T. Read, Jr., "Statistics of the Recombinations of Holes and Electrons", Physical Review, Vol. 87, p. 835, 1952.

41. F.A. Trumbore, "Solid Solubilities of Impurity Elements in Germanium and Silicon", The Bell System Technical Journal, Vol. 39, pp. 205-233, January 1960.

42. A.J. Moses, <u>Optical Materials Properties</u>, IFI/Plenum, 1971.

43. S.M. Sze, <u>Physics of Semiconductor Devices</u>, Wiley-Interscience, 1969.

FILME

2-8